THE JOURNAL OF PHYSICAL CHEMISTRY A
A JOURNAL OF THE AMERICAN CHEMICAL SOCIETY

pubs.acs.org/JPCA Article

Evaluating the Performance of the Exact Integral Simplified Time-Dependent Density Functional Theory (XsTD-DFT) to Compute One- and Two-Photon Absorption

Published as part of The Journal of Physical Chemistry A special issue "Forty Years of Response Function Theory".

Marilù G. Maraldi and Marc de Wergifosse*

Cite This: https://doi.org/10.1021/acs.jpca.5c03189 Read Online

ACCESS | Metrics & More | Article Recommendations | Supporting Information

ABSTRACT: Computing one-photon absorption and two-photon absorption (1PA and 2PA) of large molecular systems using an all-atom quantum mechanical (AQM) methodology presents significant computational challenges. This study evaluates the performance of the exact integral simplified time-dependent density functional theory (XsTD-DFT) method, a new recently introduced simplified quantum chemistry (sQC) approach that can be used as a key ingredient for AQM workflows to compute 1PA and 2PA. The *reliability*, *robustness*, and *computational efficiency* of the XsTD-DFT scheme are assessed against RI-CC2 reference calculations as well as with respect to TD-DFT results for a set of 91 organic molecules that includes systems from the QUEST database, medium-sized push−pull molecules, and small microhydrated clusters. The impact of various exchange−correlation functionals, basis sets, and the single energy threshold used to truncate the CIS space in the XsTD-DFT procedure is investigated. Results show that the XsTD-DFT method provides a substantial computational speed-up compared to TD-DFT, up to 3 orders of magnitude in CPU time with an energy threshold of 9 eV. The method robustly reproduces TD-DFT trends for excitation energies, oscillator strengths, and 2PA strengths. XsTD-DFT demonstrates reliability in capturing structure−property relationships and is reliable for nonequilibrium geometries as well as microhydrated systems. Comparisons with respect to experimental 1PA and 2PA spectra recorded in solution show similar agreements for the XsTD-DFT scheme than for TD-DFT. Guidelines for using the XsTD-DFT method in the context of 1PA and 2PA are provided. This study concludes that XsTD-DFT is a *reliable*, *robust*, and *computationally efficient* method to compute 1PA and 2PA, making it well-suited as a key ingredient for AQM workflows to treat realistic systems.

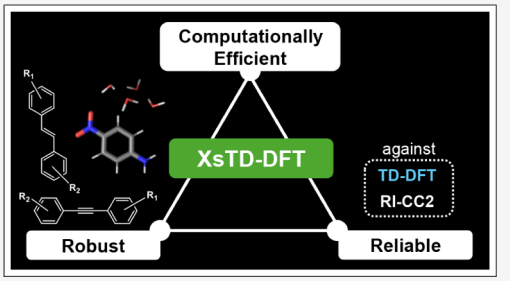

INTRODUCTION

To understand the photophysics of molecular systems, the synergy between theory and experiment has become indissoluble. Providing theoretical results directly comparable to experiments pushes the boundaries of theoretical chemistry, leading to recent developments, e.g., in the field of simplified quantum chemistry (sQC) methods.[1−3] Because molecular optical properties are strictly of a quantum mechanical (QM) nature, one needs to select an appropriate approach from the plethora of quantum chemistry methods to better balance accuracy versus computational costs. Among these properties, one-photon absorption (1PA) is routinely used by experimentalists. Since the discovery of multiphoton processes by Göppert-Mayer,[4] nonlinear optical (NLO) effects (e.g., two-photon absorption[4] (2PA)) are nowadays used as complementary experimental techniques to linear absorption.[5] 2PA allows to use a less energetic light source (in the degenerate case, one incident photon provides half of the system transition energy), unlocking improved spatial resolution,[6] reduced sample photobleaching,[7] and increased penetration depth.[8,9] These features made 2PA appealing for many applications, ranging from medicine[10] to photolithography[11] or microscopy.[12] Computationally aided design of bright 1PA and 2PA systems is an active field of research.[13−15]

Computing 2PA cross sections (σ_{2PA}) is challenging. Formally, one should evaluate the imaginary part of the third-order response function.[16] In practice, the single residue of the quadratic response provides cost-effective expressions to compute (for the degenerate case) σ_{2PA}.[16] Note that alternatively sum-over-state[17] (SOS) expressions can be used

Received: May 9, 2025
Revised: July 28, 2025
Accepted: July 28, 2025

to evaluate σ_{2PA} but depends on the whole excited state manifold. Using response functions removes the convergence problem inherent to SOS expressions, for which a large number of excited states are usually required to compute σ_{2PA}.[16,17] An appropriate method should be able to characterize excited states with different characters on the same foot. This is rather challenging because different types of excited states may require different treatments of electron correlation.[18,19]

Implementations of either the imaginary part of the cubic response function or the single residue of the quadratic response to evaluate σ_{2PA} are available for a plethora of levels of theory, including coupled cluster (CC) methods[20−23] and the density functional theory (DFT).[24,25] CCS, CCSD, CC2, RI-CC2, and CC3 methods to evaluate σ_{2PA} were implemented by Hättig et al.[20,22,23] The equation-of-motion coupled cluster singles and doubles (EOM-CCSD) method implemented by Nanda and Krylov[21] provides rather accurate 2PA results.[26,27] However, as recently shown by Naim et al.,[28] this expectation value implementation can be outperformed by the more formal quadratic response (QR) CCSD level of theory with respect to CC3. The second-order approximate coupled cluster singles and doubles (CC2) coupled with the resolution of the identity (RI-CC2) for the evaluation of the two-electron integrals is widely used as a reference for the computation of excitation energies of medium-sized systems.[29,30] The RI-CC2 method also allows for the computation of σ_{2PA} for medium-sized molecules (N_{atoms} < 100) and is usually used as a reference method to assess other levels of theory to compute 2PA strengths (δ_{2PA}).[31−34] Naim et al.[28] computed QR-CC3 reference δ_{2PA} for a set of small molecules and showed that the mean average percentage error for QR-CC2 δ_{2PA} decreases to only 26.8%, considering 2PA strengths larger than 80 a.u.

Alternatively, the time-dependent DFT (TD-DFT) is the workhorse of quantum chemistry to compute excited state properties, including 2PA.[24,25,35] In TD-DFT, the same exchange−correlation functional as for the DFT ground state is used because of the underlying adiabatic approximation.[36] This comes at the cost of a poor treatment of doubly excited states, long-range charge-transfer excitations, polarizabilities of long-chain polymers, and optical responses in solids.[37] Density functional approximations (DFAs) must be validated with respect to higher-level results. Thanks to the extensive number of TD-DFT benchmarks,[38−44] their general guidelines[30,45] can help to choose the most suited DFA for the target property. Passing from pure functionals, i.e., GGA and meta-GGA to global hybrid (GH) and range-separated hybrid (RSH) functionals, reduces the systematic underestimation of singlet-to-singlet excitation energies for a majority of systems. Common GH functionals, such as B3LYP and PBE0, give relatively good trends for valence excitation energies, providing deviations ∼0.25 eV with respect to theoretical best estimates.[30] Errors on excitation energies are usually large for CT or Rydberg states when using pure functionals. GH with a large amount of HF exchange (HFX) or RSH (e.g., CAM-B3LYP) functionals are more suited for such excited states.[3,39] $n \rightarrow \pi^*$ transitions are typically less sensitive to the choice of the DFA.[30] Regarding the evaluation of oscillator strengths and excited state dipole moments with TD-DFT, the use of GGA and meta-GGA is discouraged, and the benefit of RSH functionals over GH ones is yet unclear according to Laurent and Jacquemin.[30]

To compute δ_{2PA} with TD-DFT, no current DFA seems satisfactory with respect to CC methods.[33,46] For a set of medium-sized push−pull chromophores, Chołuj et al.[33] showed that δ_{2PA} computed using GH functionals (i.e., PBE0, B3LYP) compares better to RI-CC2 values than those obtained using pure GGA functionals (i.e., PBE, BLYP). For the same set, Ahmadzadeh et al.[34] reported that RSH functionals such as CAM-B3LYP provide strong linear correlation for δ_{2PA} values with respect to RI-CC2 ones, while GH functionals reproduce better δ_{2PA} magnitudes. According to them, the best GH GGA functional to evaluate δ_{2PA} is PBE0, with a mean relative error of around 39% with respect to RI-CC2 results for this set of compounds.[34] Note that δ_{2PA} obtained with recent hybrid meta-GGA functionals (e.g., MN15) correlate similarly with respect to RI-CC2 ones than the best RSH results from their set of DFAs. Comparable results are also obtained with GH GGA DFAs. For small molecules, Naim et al.[28] showed that the δ_{2PA} error spread with respect to QR-CC3 decreases passing from B3LYP to BHandHLYP and CAM-B3LYP. For δ_{2PA} with values larger than 80 au, the correlation with respect to QR-CC3 systematically improves for all DFAs tested. TD-DFT δ_{2PA} for transitions to Rydberg states compares the best with respect to CC3 ones. Because meta-GGA functionals are gauge-dependent, corrections were implemented to restore their invariance.[42,47] Except for M06-2X and BMK, using gauge invariance corrections for GH meta-GGA functionals does not improve the comparison with respect to the best theoretical estimate (TBE) for excitation energies from the QUEST data set.[42] In most of the cases, no general and severe effects were observed for oscillator strengths and quadratic response properties when restoring gauge invariance.[47] Typically, restoring gauge invariance to GH meta-GGA functionals improves excitation energies, oscillator strengths, and δ_{2PA} for molecules that involve pronounced out-of-plane rotation of electron density.[47−49]

After identifying the appropriate quantum chemistry method for the target optical property, two key challenges remain to simulate realistic systems: (i) accounting for environmental effects into the electronic structure calculation and (ii) incorporating dynamic structural effects.[50] For the latter, non-Condon effects[51−55] (like Franck−Condon effects or Herzberg−Teller contributions) might be important for comparison with respect to experiments, motivating the development of electronic structure methods to get vibrationally resolved 1PA and 2PA spectra.[52,56] Examples of vibronic models are the adiabatic Hessian, vertical Hessian, and vertical gradient methods.[51,57] Nevertheless, these methods can be computationally intensive. Focused models were successfully used in modern computational spectroscopy.[50,58] These models assume that the property is local. Thus, only a small region of the system is treated explicitly at a high level of theory, typically the chromophore. To account for the rest of the system, continuum solvation models provide effective environmental effects but miss specific solute−solvent interactions.[50,58] Alternatively, multiscale methods[58−60] such as QM/MM[61] enable to explicitly account for the environment at a lower level of theory (e.g., molecular mechanics (MM)). Common protocols[50] to account for dynamic structural effects include molecular dynamics (MD) simulations to explore chromophore−environment configurations[62] and compute molecular properties at each step. Ideally, these approaches require numerous QM or QM/MM calculations. Despite the success of QM/MM approaches,[59,63,64] to compute 1PA[65,66] and 2PA[67,68] properties, they still face some inherent limitations: (i) the quality of the property of the QM subsystem depends drastically on the choice of the MM force field;[69] (ii) the definition of the QM/MM boundary region can be difficult; (iii) if the Pauli repulsion of the exchange energy is

https://doi.org/10.1021/acs.jpca.5c03189
J. Phys. Chem. A XXXX, XXX, XXX−XXX

not included in the MM part, electron density leakage from the QM to the MM region can plague calculations. This problem affects in particular NLO properties.[70] Polarizable embedding models[63] or effective fragment potentials[71] (EFPs) can correct this problem, accounting for the mutual polarization of the chromophore and environment. Moreover, (iv) the convergence of the property with respect to the dimension of the QM region is system- and property-dependent.[72]

In light of these limitations, the so-called *brute-force*[58] or preferably called "*all-atom QM*"[73,74] (AQM) approach is a valid alternative. In AQM schemes, the excited states and response properties of the entire system are simply computed at the QM level. This is effectively possible thanks to recent developments in the framework of sQC methods.[73,74] Adopting an AQM approach removes the assumption that the target property is purely local. Thus, long-range effects are inherently accounted for. As for multiscale methods, different AQM protocols can be used to obtain the optical properties. An all-atom single structure QM (ASQM)[74] approach can be chosen to account exclusively for explicit environment effects. de Wergifosse and coworkers[73,75,76] successfully applied the ASQM approach to compute the second-harmonic generation[75] and 2PA of fluorescent proteins.[76] To include dynamic structural effects, two different all-atom dynamic structure QM (ADQM) protocols were proposed: (i) the ADQM-Boltz. scheme averages the optical property for a Boltzmann ensemble of conformers populated at a given temperature, and (ii) the ADQM-MD approach considers snapshots from a MD run at a QM level (e.g., GFN2-xTB[77] to provide averaged spectra).[73−76] Löffelsender et al.[74] considered the flavin mononucleotide (FMN) in a sphere of explicit water molecules as a realistic system and showed that the ADQM-MD approach provides striking agreements with respect to the experiment for 1PA and 2PA spectra of the FMN in water.

In 2013, Grimme[1] introduced the first sQC method with the simplified time-dependent density functional theory using the Tamm−Dancoff approximation (sTDA), providing a cost-efficient implementation of the TDA method using physically grounded approximations. In 2014, the simplified time-dependent density functional theory (sTD-DFT) was introduced by Bannwarth and Grimme[2] and successfully applied to compute ultraviolet/visible (UV/vis) and circular dichroism (CD) spectra of rather large molecules (<1000 atoms). The combination of both sTDA/sTD-DFT methods to an extended tight-binding (xTB) model[78] unlocked the possibility to compute excited states for ultralarge systems (<5000 atoms). Following this, de Wergifosse and coworkers extended the application of the sTD-DFT to linear and quadratic response properties, including polarizability,[79] optical rotation,[80] first hyperpolarizability,[79] excited-state absorption,[81] and two-photon absorption.[76] A spin-flip version[82] of the sTD-DFT scheme was also implemented. References 73 and 83 review such developments.

The sTDA and sTD-DFT schemes were inspired by early semiempirical quantum chemistry methods. While the DFT ground state is computed without further approximations, the excited state/response calculation relies on three main simplifications of TD-DFT Casida's equations.[36,84] First, the terms that depend on the linear response of the exchange−correlation potential (i.e., $\frac{\delta v_{xc}}{\delta \rho(\mathbf{r})} = f_{xc}$) are neglected from **A** and **B** supermatrices in a random phase approximation fashion.[85] The second approximation allows a cost-efficient four-index transformation of the atomic orbital (AO) two-electron integrals into the molecular orbital (MO) space to compute **A** and **B** supermatrices. For this, the zero-differential approximation (ZDO)[86,87] common in early-stage semiempirical methods is applied. For each atom (A), transition charges (Q_A^{ia}) are collected using a Löwdin orthonormalization procedure:[86,88]

$$Q_A^{ia} = \sum_{\alpha \in A} C_{\alpha i}^{\text{low}} {}^{*} C_{\alpha a}^{\text{low}} \tag{1}$$

where $C_{\alpha a}^{\text{low}}$ are Löwdin-orthogonalized LCAO coefficients. Assuming that Löwdin-orthogonalized orbitals (LOs) are atom-centered, Löwdin-orthogonalized two-electron integrals are collected for atoms A and B as

$$(AA|BB) = \sum_{\alpha \in A, \beta \in B} (\lambda_\alpha \lambda_\alpha | \lambda_\beta \lambda_\beta) \tag{2}$$

Two-electron integrals are approximated using a damped Coulomb law[1,2] using the MNOK damped Coulomb operator[89−91] for exchange integrals:

$$(AA|BB)^K = \left(\frac{1}{(R_{AB})^{y_K} + (\frac{\eta_A + \eta_B}{2})^{-y_K}} \right)^{1/y_K} \tag{3}$$

and for Coulomb integrals:

$$a_x (AA|BB)^J = \left(\frac{1}{(R_{AB})^{y_J} + (a_x \frac{\eta_A + \eta_B}{2})^{-y_J}} \right)^{1/y_J} \tag{4}$$

where R_{AB} is the interatomic distance, y_K and y_J are linear functions of a_x, and η_A is the chemical hardness of atom A. Approximated MO two-electron integrals are obtained as

$$(ia|jb) \approx \sum_{AB} Q_A^{ia} Q_B^{jb} (AA|BB) \tag{5}$$

In this way, sTD-DFT/sTDA computation times scale with the number of atoms. Third, to truncate the space of singly excited configuration state functions (CSFs), a single energy threshold, E_{thr} that represents the spectral range of an excited state calculation, is used. The complete description of the procedure can be found in the reference 73. In addition to these three main simplifications, quadratic response functions are further simplified by neglecting the Hartree exchange−correlation kernel and the second derivative of the exchange−corelation potential (i.e., $\frac{\delta f_{xc}}{\delta \rho(\mathbf{r})} = g_{xc}$).

To remove the semiempiricism characterizing the evaluation of two-electron integrals in sQC methods, one of us[3,73,92] recently introduced the eXact integral sTD-DFT (XsTD-DFT), where exact two-center atomic orbital two-electron integrals $(\alpha\alpha|\beta\beta)$ are used instead of MNOK ones. In the XsTD-DFT scheme, MO two-electron integrals are approximated as

$$(ij|ab) \approx \sum_{\alpha,\beta} Q_\alpha^{ia} Q_\beta^{jb} (\alpha\alpha|\beta\beta) \tag{6}$$

where transition charges Q_α^{ia} are collected for each basis function α. The performance of the TDA variant of the XsTD-DFT scheme (XsTDA)[92] to compute excited states was assessed for a set of 77 molecules. XsTDA results were compared to TDA results using GH functionals (B3LYP, PBE0, BHandHLYP, and M06-2X). With respect to TDA, the XsTDA method was more

https://doi.org/10.1021/acs.jpca.5c03189
J. Phys. Chem. A XXXX, XXX, XXX−XXX

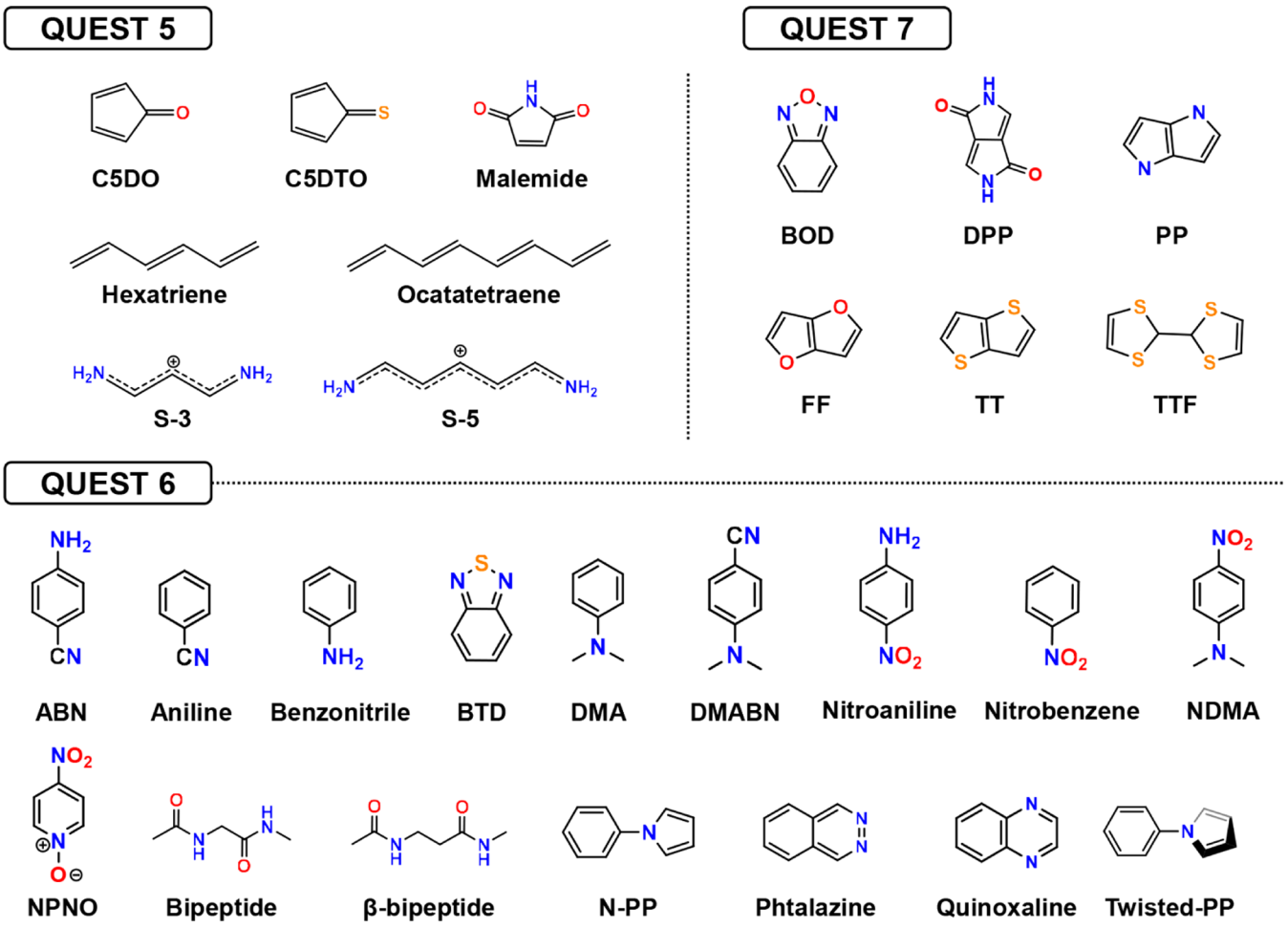

Figure 1. Chemical structures selected from QUEST 5,[94] QUEST 6,[95] and QUEST 7[96] databases (C5DO = cyclopentadienone, C5DTO = cyclopentadienthione, S-3 (S-5) = streptocyanine-c3(5), ABN = aminobenzonitrile, DMA = dimethylaniline, DMABN = dimethilaminobenzonitrile, NDMA = nitrodimethylaniline, NPNO = nitropyridine *N*-oxide, N-PP = *N*-phenylpyrrole, Twisted-PP = twisted *N*-phenylpyrrole, BOD = benzoxadiazole, DPP = diketopyrrolopyrrole, BTD = benzothiadiazole, PP = pyrrolopyrrole, FF = furofuran, TT = thienothiophene, TTF = tetrathiafulvalene).

robust than sTDA at reproducing excitation energies, especially when using functionals with large amounts of HFX. For example, a MAD of 0.35 eV was obtained with XsM06-2X, much smaller than the sTDA one of 0.74 eV. Regarding oscillator strengths, XsTDA MADs were also less spread with respect to the full scheme than for sTDA, particularly for large oscillator strength values. Among the results, $n \rightarrow \pi^*$ transitions are not well described by both XsTDA and sTDA schemes because the inherent ZDO approximation in those schemes neglects one-center exchange integrals $(\alpha_A\beta_A|\alpha_A\beta_A)$. Interestingly, the first one-photon-active Rydberg $n \rightarrow \mathrm{Ry}(3s)$ transition of acetone was well reproduced by the XsTDA method. TDA excitation energies and oscillator strengths for CT states were robustly reproduced by XsTDA outperforming sTDA, especially when considering a large amount of HFX. Using an E_{thr} value of 9 eV to truncate the CI space, the XsTDA scheme is 20 times faster than the full scheme on average, while the sTDA speed-up is around 100. Note that errors in excitation energies decrease when enlarging the size of the system, an interesting feature for a method designed to describe large systems. Regarding 2PA, both sTD-DFT and XsTD-DFT schemes using B3LYP provided excellent comparisons with respect to experiments to reproduce the 2PA spectrum of eGFP using a model system that includes the deprotonated chromophore and its first shell of surrounding residues (359 atoms).[92] Accounting explicitly for the whole protein as well as dynamic structural effects should reduce the gap between the XsTD-DFT and experimental 2PA spectra. This will be the subject of future studies applying the XsTD-DFT scheme to realistic systems.

Last year, one of us[3] extended the reach of both XsTDA and XsTD-DFT schemes to RSH functionals. Note that Risthaus et al.[93] provided parameters for the sTD-DFT scheme to use a ground state determined with a RSH functional, but sTD-DFT equations are still solved for the GH case. Because XsTD-DFT and XsTDA schemes use exact two-electron integrals, it is now possible to solve Casida's equations for the RSH case with these methods. Among the results, de Wergifosse[3] showed that the XsCAM-B3LYP scheme can reproduce the shape and relative intensities of the experimental 1PA and CD spectra of the photoactive yellow protein (PYP) using the entire protein (1931 atoms) for the calculation in an ASQM fashion. One of the main transitions necessary to reproduce both spectra is associated with a local $\pi \rightarrow \pi^*$ transition located on a tryptophan from the protein. This result advocated for the use of an AQM approach to correctly represent excited-state properties of such ultralarge systems.

For the moment, the sTD-DFT-xTB scheme has not been extended to the XsTD-DFT level of theory because MO

https://doi.org/10.1021/acs.jpca.5c03189
J. Phys. Chem. A XXXX, XXX, XXX−XXX

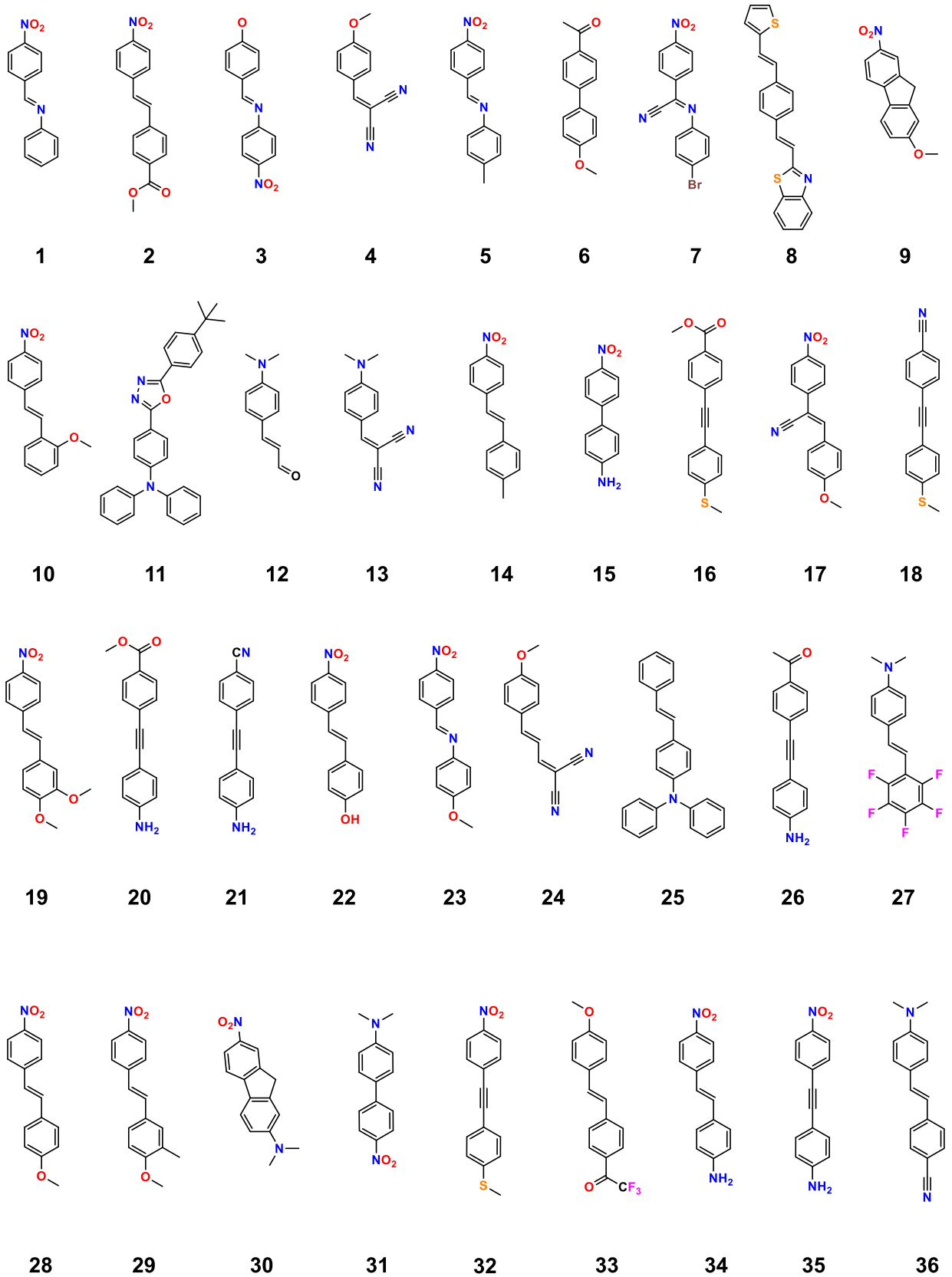

Figure 2. Chemical structures of the first 36 push−pull molecules taken from the CT set.[33]

energies from the xTB ground state are arbitrarily shifted to provide better HOMO−LUMO gaps. In the sTD-DFT-xTB scheme, semiempirical two-electron integrals are fitted to absorb this arbitrary correction. At the XsTD-DFT level, this is not possible because integrals are computed exactly. Thus, the xTB scheme cannot be directly used as it is with the XsTD-DFT scheme.

https://doi.org/10.1021/acs.jpca.5c03189
J. Phys. Chem. A XXXX, XXX, XXX−XXX

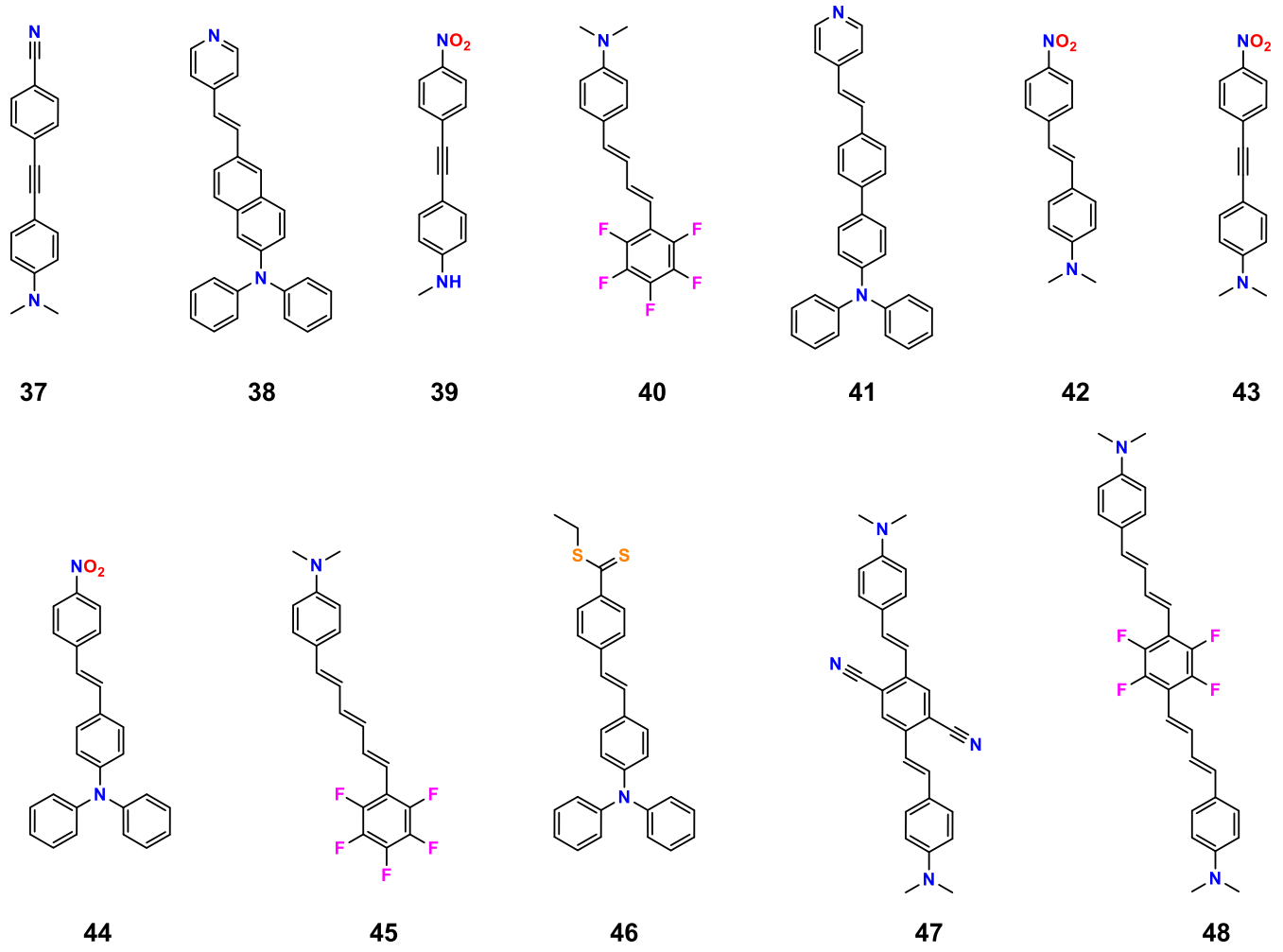

Figure 3. Chemical structures of the 37−48 push−pull molecules taken from the CT set.[33]

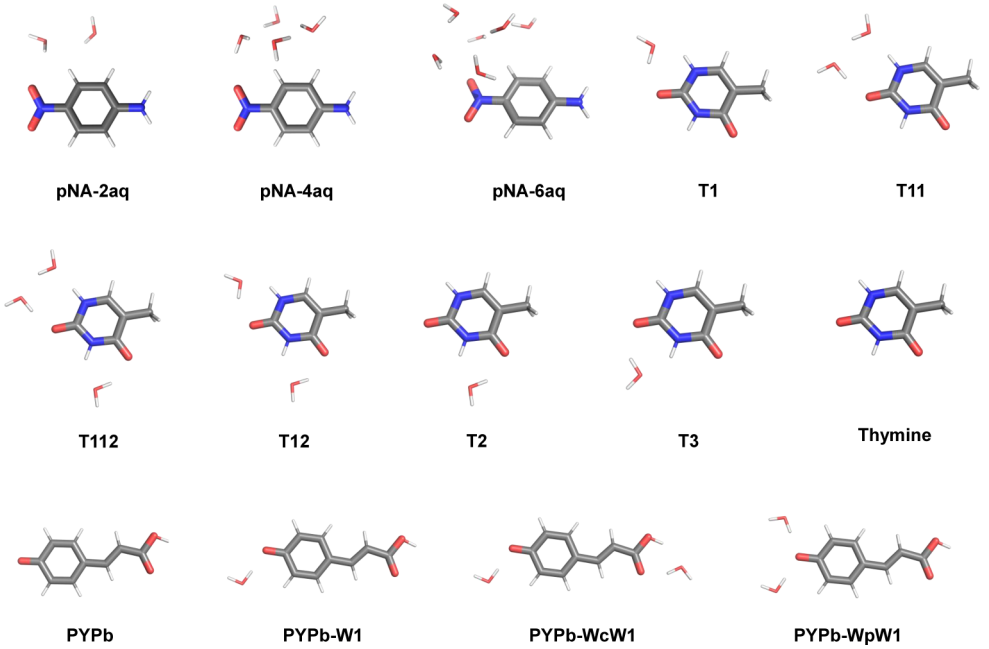

Figure 4. Chemical structures for microhydrated clusters involving para-nitroaniline, thymine, and the photoactive yellow protein chromophore from reference.[69]

https://doi.org/10.1021/acs.jpca.5c03189
J. Phys. Chem. A XXXX, XXX, XXX−XXX

The use of sQC schemes as core methods to compute excited state and response properties for large systems in AQM approaches places them as robust candidates to bridge the gap between experimental and computational electronic spectroscopy. First results[3,92] obtained at both XsTDA and XsTD-DFT levels of theory to compute 1PA and 2PA motivate us to assess systematically and more extensively the XsTD-DFT scheme, considering GH and RSH functionals. The main goal of this study is to assess the performance of the XsTD-DFT method to compute excitation energies as well as oscillator and 2PA strengths of organic compounds. An ideal sQC method used in an AQM procedure to evaluate 1PA and 2PA should be (i) *reliable*, providing results directly comparable to a reference or experiment; (ii) *robust*, performing consistently across different types of systems, being widely applicable, and requiring minimal parameter tuning while demonstrating good error tolerance; and (iii) *computationally efficient*, being able to solve with reasonable timings the electronic structure problem for large systems within AQM methodologies. 91 molecular systems were selected from different studies[33,69,94−96] to assess that the XsTD-DFT method satisfies such criteria when computing 1PA and 2PA. These sets include selected systems from the QUEST database[94−96] for which Jacquemin and co-workers[94] collected highly accurate theoretical excitation energies and oscillator strengths, i.e., TBEs. Only the largest systems from the QUEST database, namely QUEST 5,[94] QUEST 6,[95] and QUEST 7[96] were selected because the XsTD-DFT scheme has been designed to treat large systems (Figure 1). QUEST 5 and 7 sets[94,96] concern molecules reporting singlet excited states mainly of valence ($\pi \rightarrow \pi^*$, $n \rightarrow \pi^*$) and Rydberg character. The QUEST 6 set[95] involves transitions with an intramolecular charge transfer (CT) character. Because detectable 2PA strengths are generally on the order of at least 100 a.u.,[97] we included 48 medium-sized push−pull molecules (up to 64 atoms) from Zaleśny and co-workers[33] (Figures 2 and 3). They reported two-photon (2P) allowed excitations of CT nature with large strengths (between 10^3 and 10^6 a.u.). Throughout this work, this database is referred to as the "CT set". The impact of local solvation on 1PA and 2PA is also assessed using 12 microhydrated clusters of para-nitroaniline (pNA), thymine (T), and photoactive yellow protein chromophore (PYPb) taken from references[98,99,100] (Figure 4). Reference EOM-EE-CCSD/6-31+G(d) excitation energies as well as oscillator and 2PA strengths are available for these systems.[69]

The RI-CC2 scheme was selected as a reference method to assess the performance of the XsTD-DFT scheme. Deviations with respect to the full TD-DFT scheme as well as the sTD-DFT[1,2] method are also discussed. To validate the use of the RI-CC2 scheme as a reference, we report in Figure S1 correlation plots between RI-CC2/aug-cc-pVDZ and TBE excitation energies ($E_{S_0 \rightarrow S_n}$) and oscillator strengths ($f_{S_0 \rightarrow S_n}$) computed for 80 singlet-to-singlet excitations from the QUEST database. The spread of the excitation energy correlation plot between RI-CC2 and TBEs is rather contained. Table S1 reports an overall mean absolute deviation (MAD) of 0.13 eV with respect to the TBE for excitation energies and a MAD of 0.018 for oscillator strengths. Oscillator strengths' MADs divided into three classes are also reported (Table S1). They are defined according to the range of magnitudes for TBE oscillator strengths: c_1 for $f_{0\rightarrow n}^{\mathrm{TBE}} \in]0.02, 0.10]$, c_2 for $f_{0\rightarrow n}^{\mathrm{TBE}} \in [0.10, 1.0]$, and c_3 for $f_{0\rightarrow n}^{\mathrm{TBE}} > 1.0$. For each class, we obtained MAD values of 0.01, 0.04, and 0.17, respectively. For each class, we also observed zero or positive mean deviations (MDs), i.e., 0.00, +0.03, and +0.17 for c_1, c_2, and c_3, respectively. These results show that the small RI-CC2 oscillator strengths compare better to the TBE ones (i.e., c_1 and c_2). RI-CC2 also tends to overestimate large oscillator strengths (i.e., c_3). Our results as well as previous works[29−34] show that the RI-CC2 method seems reliable enough to be used as a theoretical reference for such excited states, especially for medium-sized systems for which more accurate wave function methods cannot be applied.

As discussed above, the main goal of this study is to show that the XsTD-DFT method is a *computationally efficient*, *reliable*, and *robust* method to evaluate 1PA and 2PA. Regarding computational times, comparisons are made using TD-DFT, sTD-DFT, and XsTD-DFT schemes to compute 2PA strengths for 20 excited states using the aug-cc-pVDZ basis set (BS). XsTD-DFT's *robustness* and *reliability* to compute excitation energies, 1PA and 2PA strengths, are discussed in comparison with TD-DFT and RI-CC2 methods. The performances in computing 1PA and 2PA are systematically assessed for different DFAs: TPSSH, B3LYP, PBE0, M06, M06-2X, BHandHLYP, CAM-B3LYP, ωB97X-D3, and ωB97M-V. Basis set effects are also discussed for different double-ζ basis sets. We compare XsTD-DFT/BS and sTD-DFT/BS results with respect to TD-DFT/BS as well as RI-CC2/aug-cc-pVDZ results, providing a systematic study on BS effects for sQC methods. We also studied the impact of the truncation of the CIS space using a single energy threshold on excitation energies, as well as oscillator and 2PA strengths. The convergence of XsTD-DFT results toward the TD-DFT limit is assessed when systematically varying E_{thr} from 7 to 45 eV, using different DFAs, i.e., PBE0, M06-2X, CAM-B3LYP, and ωB97M-V. Finally, the *robustness* of the XsTD-DFT method was further investigated to relate structures to computed optical properties. The present study provides answers to the following questions: (1) is the XsTD-DFT method able to capture trends on optical properties upon changing geometries with respect to the full scheme as well as RI-CC2 reference calculations? (2) How does the XsTD-DFT scheme perform for nonequilibrium geometries? (3) Are XsTD-DFT 1PA and 2PA results reliable for microsolvated systems, and how does it perform with respect to other methods such as EOM-EE-CCSD, TD-DFT, sTD-DFT, sTD-DFT-xTB, QM/QM, and QM/MM? (4) How do XsTD-DFT (and TD-DFT) results in vacuum for excitation energies as well as oscillator and 2PA strengths compared to experiments recorded in solution? (5) How do these comparisons to experiments change when using the XsTD-DFT method with an implicit solvent model?

This paper is structured as follows: after a description of the computational details, we discuss results and provide conclusions as well as outlooks.

METHODS

In this study, 1PA and 2PA of 91 compounds are investigated: QUEST (Figure 1), CT (Figures 2 and 3), and microhydrated clusters (Figure 4) sets. Geometries at CC3/(aug-)cc-pVTZ or CCSD(T)/cc-pVTZ levels of theory were taken from the QUEST database.[94−96] Some systems were excluded for the reasons provided in Table S2. Structures from the CT set were taken from ref. 33, and they were optimized at the B3LYP/cc-pVTZ level by Zaleśny and coworkers[33] (Figures 2 and 3). The microhydrated geometries of pNA, thymine, and PYPb were taken from Nanda and Krylov[69] (Figure 4). For the QUEST set, TBEs of excitation energies and oscillator strengths were taken

https://doi.org/10.1021/acs.jpca.5c03189
J. Phys. Chem. A XXXX, XXX, XXX−XXX

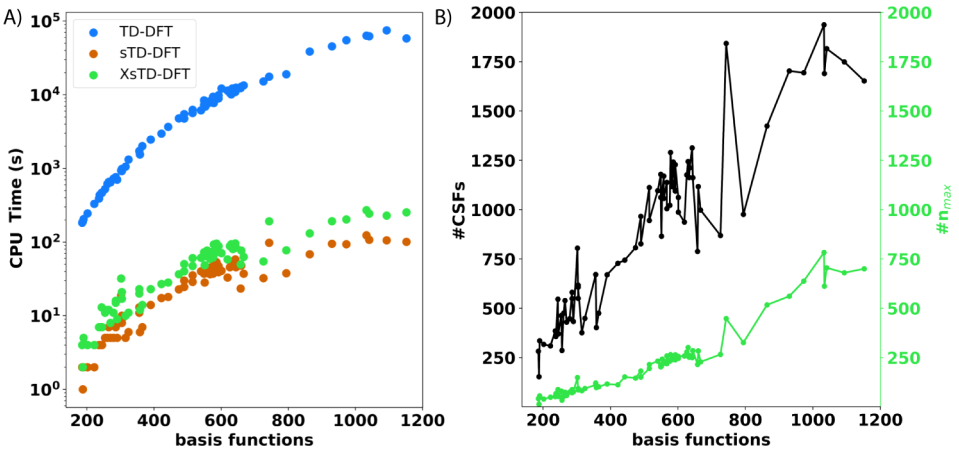

Figure 5. CPU times (s) to compute 2PA strengths at the TD-DFT level with `TURBOMOLE` as well as sTD-DFT and XsTD-DFT levels with the `std2`[101] program using the B3LYP exchange−correlation functional and the aug-cc-pVDZ basis set as a function of the number of basis functions (left panel). Twenty excited states were computed for each system at the TD-DFT level, while for simplified methods, the number of states ($\#n_{max}$, right panel) was imposed by the energy threshold of 9 eV; 2PA strengths were only computed for the first 20 excited states. The number of states ($\#n_{max}$) and the total number of CSFs involved in (X)sTD-DFT calculations are reported in the right panel.

from Jacquemin and coworkers.[94−96] For the CT set, RI-CC2/aug-cc-pVDZ reference excitation energies as well as oscillator and 2PA strengths were taken from Chołuj et al.[33] EOM-EE-CCSD/6-31+G(d) reference values were taken from ref. 69 for microhydrated clusters.

We performed TD-DFT, sTD-DFT, and XsTD-DFT excited state and 2PA calculations for different GH and RSH exchange−correlation functionals (in order of increasing amounts of HFX): TPSSH (10%), B3LYP (20%), PBE0 (25%), M06 (27%), BHandHLYP (50%), and M06-2X (54%) as well as RSH with and without dispersion correction (i.e., CAM-B3LYP, ωB97X-D3, and ωB97M-V). These popular DFAs are directly available in the implementation of (X)sTD-DFT approaches in the `std2`[101] program, except for sωB97M-V for which the sTD-DFT parametrization is not available. Note that for meta-GGA hybrids, gauge-invariance corrections do not apply to (X)sTD-DFT calculations because f_{xc} is neglected. All meta-GGA hybrid TD-DFT excitation energy and oscillator strength calculations are corrected for gauge-invariance by default using `Turbomole 7.6`.[47,102] Support for gauge-invariant meta-GGA hybrids for 2PA cross sections was made available since `Turbomole 7.8`.[47] For a few systems from the QUEST set, comparisons between 2PA strengths computed with and without gauge-invariance correction can be found in the spreadsheet that accompanies the Supporting Information for TPSSH, M06, M06-2X, and ωB97M-V exchange−correlation functionals. These results indicate that restoring gauge invariance negligibly impacts the 2PA strengths. Basis set effects are investigated for various double-ζ: 3-21G(d), 6-31G(d), cc-pVDZ, def2-SVP, 6-31+G(d), and aug-cc-pVDZ. For completeness, sTD-DFT-xTB[78] results are compared as well to RI-CC2/aug-cc-pVDZ ones.

Simplifications in (X)sTD-DFT schemes are designed to reduce the computational cost of TD-DFT. Figure 5 reports the CPU times required to compute the first 20 2PA strengths at TD-DFT, sTD-DFT, and XsTD-DFT levels (B3LYP DFA) as a function of the number of basis functions. With both sTD-DFT and XsTD-DFT methods, we gain for the largest systems 3 orders of magnitude in CPU times on a 16-CPU computer node (Intel Xeon E5-2650 v2, 2.60 GHz). For the largest system of the database (molecule 48), linear and quadratic responses were computed in 971, 4, and 2 min of CPU time at TD-DFT, XsTD-DFT, and sTD-DFT levels of theory, respectively.

For the statistical analysis of linear absorption properties, we selected the first significantly bright excited states (i.e., oscillator strength >0.020) at the RI-CC2/aug-cc-pVDZ level for each molecule. The corresponding TD-DFT, sTD-DFT, and XsTD-DFT excited states are assigned based on their transition energy ($E_{0\to n}$, in eV) and oscillator strengths ($f_{0\to n}$). For the difficult assignments from QUEST molecules, we relied on the symmetry of the excited states, as well. Symmetry considerations are not accounted for in the `std2`[101] program, so they are not applicable to (X)sTD-DFT state assignments. As we did in the introduction, when comparing RI-CC2 results to TBEs, oscillator strengths from the QUEST database (Table S3) are divided into three classes according to their ranges of magnitude at the RI-CC2/aug-cc-pVDZ level: $\{c_1|f \in]0.02;0.1]\}$, $\{c_2|f \in [0.1;1.0]\}$, and $\{c_3|f > 1.0\}$. The excited states from the CT set show oscillator strength values larger than 0.5 at the RI-CC2/aug-cc-pVDZ level of theory, with the exception of systems 1 (f = 0.29, Figure 2), 47, and 48 (Figure 3, both f = 0.00, which are excluded from the statistical analysis for 1PA). Thus, we do not report any classes of oscillator strengths for the CT set.

Throughout this work, microscopic rotationally averaged 2PA strengths δ^{2PA} are reported in atomic units. Unlike 2PA macroscopic cross sections (Göppert-Mayer units), δ^{2PA} provides an unambiguous descriptor for comparing computational methods because it is independent of experiment-specific factors.[26,27,31] In the case of two degenerate linearly polarized incident photons $\left(\omega_1 = \omega_2 = \frac{\omega_n}{2}\right)$, δ^{2PA} is computed as the sum over Cartesian components ($\eta,\zeta \in \{x,y,z\}$) of 2PA transition moments ($S^{0\to n}$) between the ground and n states:

$$\delta^{2PA} := \langle \delta_{//}^{2PA} \rangle = \frac{1}{15} \sum_{\zeta\eta} (S_{\zeta\zeta} S_{\eta\eta}^{*} + S_{\zeta\eta} S_{\zeta\eta}^{*} + S_{\zeta\eta} S_{\eta\zeta}^{*}) \quad (7)$$

The SOS expression for transition moment components ($S_{\zeta\eta}$ and their complex conjugate) considering two degenerate incident photons $\left(\frac{\omega_n}{2}\right)$ is given as follows:

https://doi.org/10.1021/acs.jpca.5c03189
J. Phys. Chem. A XXXX, XXX, XXX−XXX

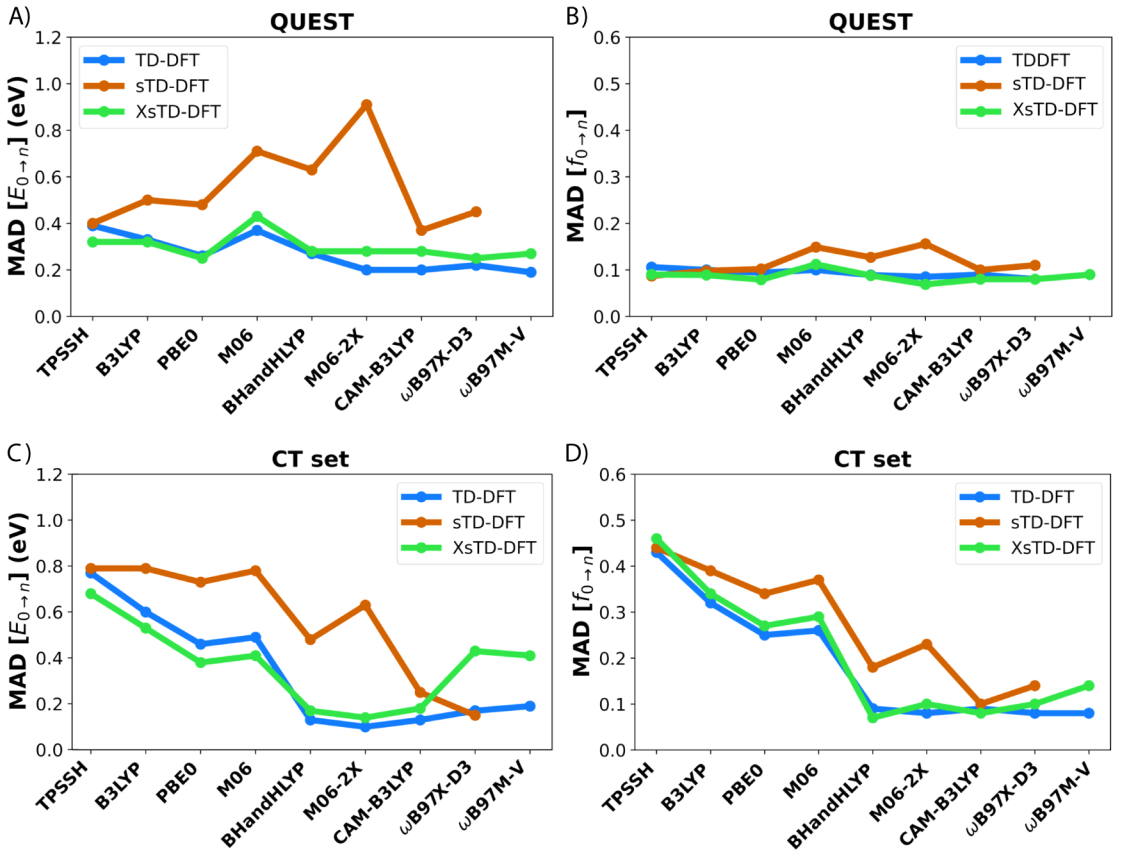

Figure 6. For both QUEST and CT sets, MADs for excitation energies and oscillator strengths computed at TD-DFT, sTD-DFT, and XsTD-DFT levels of theory using TPSSH, B3LYP, PBE0, M06, BHandHLYP, M06-2X, CAM-B3LYP, ωB97X-D3, and ωB97M-V exchange−correlation functionals with respect to the RI-CC2 results using the aug-cc-pVDZ basis set.

$$S_{\zeta\eta}^{0\to n} = \sum_{i\neq n} \frac{\langle 0|\hat{\mu}_\zeta|i\rangle\langle i|\hat{\mu}_\eta - \langle 0|\hat{\mu}_\eta|0\rangle|n\rangle}{\omega_i - \frac{\omega_n}{2}} + \frac{\langle 0|\hat{\mu}_\eta|i\rangle\langle i|\hat{\mu}_\zeta - \langle 0|\hat{\mu}_\zeta|0\rangle|n\rangle}{\omega_i - \frac{\omega_n}{2}} \quad (8)$$

where $\langle 0|\hat{\mu}_\zeta|i\rangle$ are transition dipole moments along the ζ axis and $\hat{\mu}_\zeta - \langle 0|\hat{\mu}_\zeta|0\rangle$ is the fluctuation operator. For details about the conversion from microscopic strengths to macroscopic cross sections, the interested reader is referred to refs. 26, 31, and 27 and the Supporting Information. 2P-active states were selected as for 1PA based on the first dominant 2PA bright state in nonresonant conditions. For these sets of organic molecules, we excluded high-energy excited states (above 6 eV) motivated by the spectral ranges typically used for 2PA experiments.[103] Note that when two excited states have a difference of excitation energies below or equal to 0.05 eV, they were considered as nearly degenerate and their excitation energies were averaged, while corresponding oscillator strengths and 2PA strengths were summed up. The QUEST database is composed of molecules that report δ^{2PA} between 10^0 and 10^4 (in a.u.), while CT set systems exhibit $\delta^{2PA} \in [10^3, 10^7]$ a.u. 2PA strengths are reported on a logarithmic scale ($log(\delta^{2PA})$). This allows one to compare method performance according to the δ^{2PA} order of magnitude.

Symmetry-related selection rules are not the same for 1P- and 2P-active states.[27,104] For 1PA, group theory imposes that the direct product between irreps of the ground state, the electric dipole operator, and the excited state belongs to the totally symmetric irreps. For 2PA, the dipole moment operator is involved twice in numerators of the SOS expression (eq 8). Thus, both 2P-active transitions to intermediate states should belong to the totally symmetric irreps, and to be 2P-active, the state should have at least one 1P-active intermediate state.[27,104] As a result, 2P transitions between states connected by a large number of virtual states should in principle exhibit large 2PA transition moments (eq 8). Destructive interference between optical channels can decrease the final 2PA strength value.[105] Optical channel interference is hidden in the response theory formalism but can be described with the generalized few-state-model approach.[105] For push−pull molecules of C_1 symmetry from the CT set, the 1P-active states are also 2P-bright. This is not necessarily the case for the QUEST set because most of the molecules belong to higher symmetry point groups. For each molecule of the QUEST set, we selected the first significant 2P-bright state off-resonance (i.e., with respect to the first 1PA-active state) with an excitation energy below 6 eV.

RI-CC2 and TD-DFT calculations were performed with `Turbomole 7.6.1`[102] software. Extra RI-CC2/aug-cc-pVDZ excitation energies, f, and δ^{2PA} for the CT set were taken from the reference 33. The `std2`[101] program was used to perform sTD-DFT and XsTD-DFT calculations. All (X)sTD-DFT computations were fed with DFT ground-state molecular orbitals and their energies computed with `Q-Chem 6.0.1.2`.[106] Note that DFT ground-state calculations were always followed by an internal stability analysis to verify whether the calculation converged to a proper SCF energy minimum. The (99,590) DFT numerical grid from `Q-Chem` was adopted. Only sTD-DFT-xTB calculations used xTB molecular orbitals

https://doi.org/10.1021/acs.jpca.5c03189
J. Phys. Chem. A XXXX, XXX, XXX−XXX

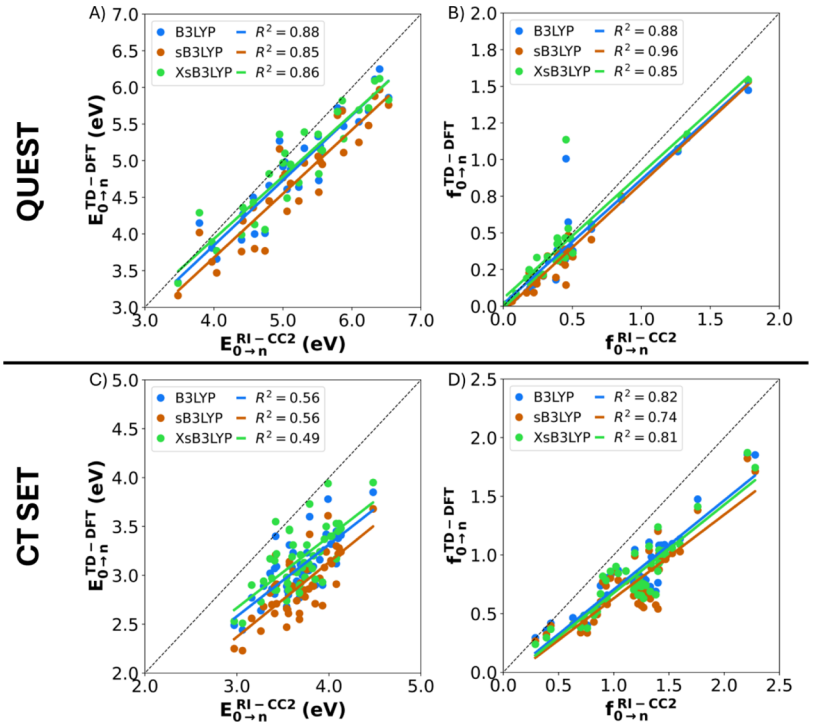

Figure 7. For both QUEST and CT sets, correlation plots of excitation energies and oscillator strengths for TD-DFT, sTD-DFT, and XsTD-DFT levels using the B3LYP DFA and with respect to the RI-CC2 one using the aug-cc-pVDZ basis set. Linear regression R^2 values are given for each method.

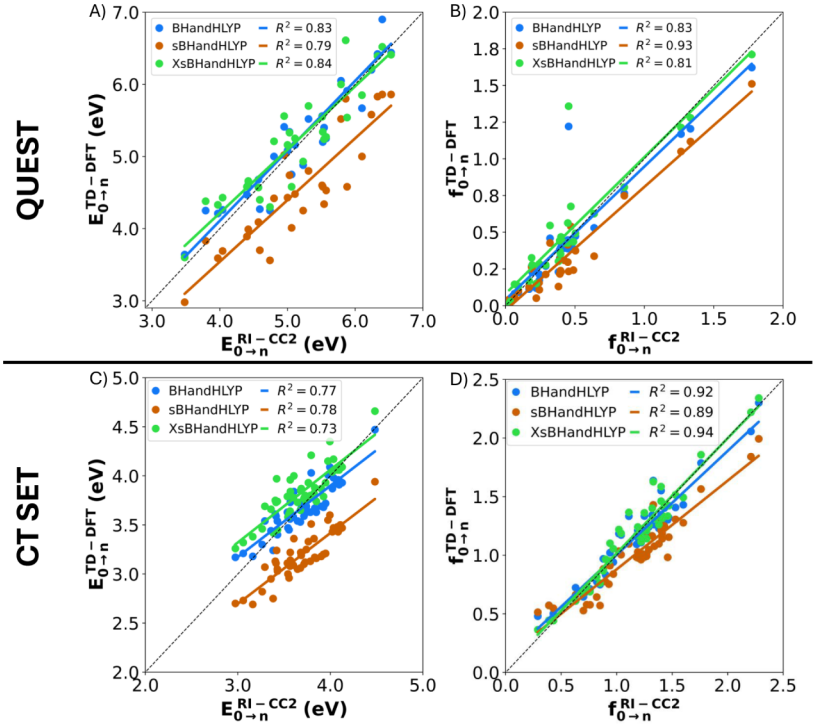

Figure 8. For both QUEST and CT sets, correlation plots of excitation energies and oscillator strengths for TD-DFT, sTD-DFT, and XsTD-DFT levels using the BHandHLYP DFA and with respect to the RI-CC2 one using the aug-cc-pVDZ basis set. Linear regression R^2 value are given for each method.

computed with the `xtb4stda 1.0`[101] program. If not mentioned otherwise, we used an E_{thr} value of 9 eV to truncate the space of the CSFs. `std2` uses the `libcint`[107] library to compute analytical Gaussian-type orbital (GTO) one- and two-electron integrals.

RESULTS AND DISCUSSION

In this section, the performances of the XsTD-DFT, sTD-DFT, and TD-DFT methods to compute excitation energies, oscillator, and 2PA strengths are assessed with respect to RI-

https://doi.org/10.1021/acs.jpca.5c03189
J. Phys. Chem. A XXXX, XXX, XXX−XXX

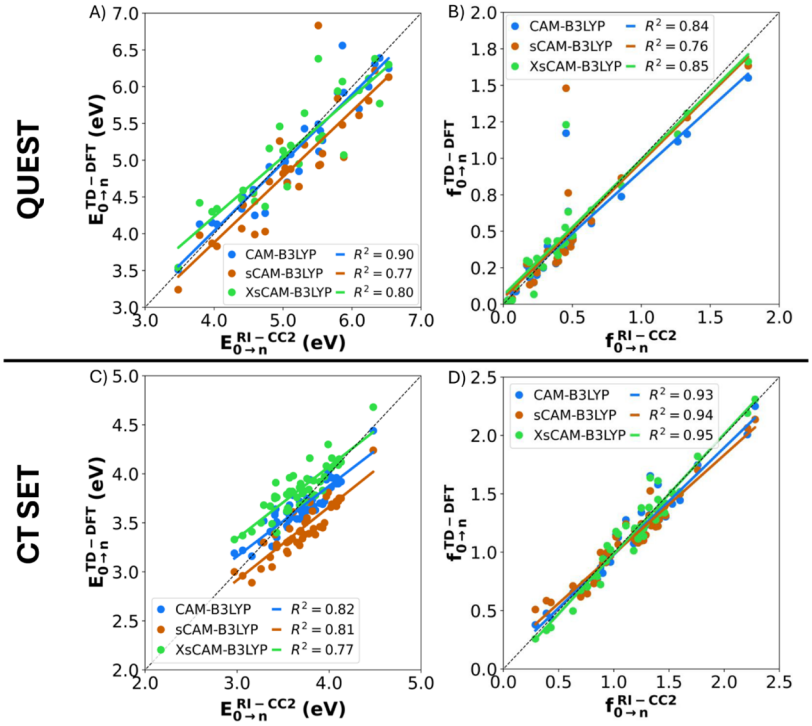

Figure 9. For both QUEST and CT sets, correlation plots of excitation energies and oscillator strengths for TD-DFT, sTD-DFT, and XsTD-DFT levels using the CAM-B3LYP DFA and with respect to the RI-CC2 one using the aug-cc-pVDZ basis set. Linear regression R^2 values are given for each method.

CC2 reference values. For 1PA and 2PA, the analysis explores the effects of different DFAs, the choice of the basis set, and the impact of the single energy threshold to reproduce the reference values. Both benchmark sets (QUEST and CT) are discussed. The QUEST set involves small organic molecules with excited states of different characters $n \to \pi^*$, $\pi \to \pi^*$, Rydberg, etc. The CT set encompasses medium-sized push−pull π-conjugated organic molecules with excited states of CT character. The CT set gives the opportunity to study subsets of substituted stilbene, para-substituted benzalanine, and substituted bisphenylacetylene molecules as well as compounds with cyanide groups. For completeness, the influence of compound 1's dihedral angle on 1PA and 2PA is investigated to assess the performance of the XsTD-DFT scheme to treat nonequilibrium geometries. Following this, the robustness of the XsTD-DFT approach is challenged for microhydrated systems. Finally, the gas-phase and implicit solvation 1PA and 2PA results are directly compared to available experiments recorded in solution.

One-Photon Absorption. For the QUEST and CT sets, Figure 6 reports MADs for TD-DFT, sTD-DFT, and XsTD-DFT from RI-CC2 reference values. MADs are reported for $E_{0\to n}$ (in eV) and $f_{0\to n}$ considering different GH and RSH exchange−correlation functionals. Tables S3 and S4 display MAD values for the QUEST and CT sets, respectively. XsTD-DFT MADs (for 77 excited states) closely follow TD-DFT ones with respect to RI-CC2 for both sets. Larger MADs of 0.43 and 0.41 eV are obtained for ωB97X-D3 and ωB97M-V, considering the CT set. We will see in the section about the selection of E_{thr} that the XsTD-DFT scheme using RSH DFAs needs a larger E_{thr} value to be converged. For both sets, the sTD-DFT method provides larger MADs with respect to RI-CC2, especially for GH functionals with a large amount of HFX ($a_x \geq 0.5$).

For QUEST and CT sets, correlation plots with respect to RI-CC2 references for excitation energies and oscillator strengths computed at the TD-DFT, sTD-DFT, and XsTD-DFT levels of theory are shown in Figures S2 (TPSSH), 7 (B3LYP), S3 (PBE0), S4 (M06), S5 (M06-2X), 8 (BHandHLYP), 9 (CAM-B3LYP), S6 (ωB97X-D3), and S7 (ωB97M-V). Both sets encompass different ranges of excitation energies (QUEST: ∼3 eV−7 eV and CT: ∼3 eV−4.5 eV). Considering GH DFAs with a low amount of HFX (B3LYP: Figure 7 and PBE0: Figure S3), TD-DFT and XsTD-DFT excitation energies tend to be underestimated with respect to RI-CC2 ones, especially for the CT set. Excitation energies at TD-DFT and XsTD-DFT levels are more spread with respect to the reference, with RMSDs of 0.64 and 0.57 eV for B3LYP and XsB3LYP as well as 0.50 and 0.43 eV for PBE0 and XsPBE0, respectively (see Table S5). From 10 to 27% of HFX, TD-DFT and XsTD-DFT excitation energy MADs for the QUEST set are globally lower (<0.5 eV) than for the CT set (MADs ∈]0.4, 0.8[eV). Using GH DFAs with a larger amount of HFX (e.g., BHandHLYP: Figure 8 and M06-2X: Figure S5) provides better correlations of excitation energies with respect to RI-CC2 ones for TD-DFT and XsTD-DFT schemes, with MADs of 0.13 and 0.17 eV for BHandHLYP and XsBHandHLYP, respectively (see Table S4). This is not the case for sTD-DFT that systematically underestimates RI-CC2 excitation energies. Using RSH exchange−correlation functionals (e.g., CAM-B3LYP: Figure 9 and ωB97X-D3: Figure S6), the XsTD-DFT method overestimates excitation energies obtained with both TD-DFT and RI-CC2 methods (Figure 9), especially for the CT set. For XsCAM-B3LYP, XsωB97X-D3, and XsωB97M-V, MADs are 0.18, 0.43, and 0.41 eV, respectively (Table S4). For the QUEST set, XsTD-DFT MADs ∼0.3 eV using RSH functionals are comparable to those from GH functionals with large amounts of HFX. Even at the TD-DFT level, the MAD with respect to RI-CC2 is not diminished when passing from GH exchange−correlation functionals with a large amount of HFX to RSH

https://doi.org/10.1021/acs.jpca.5c03189
J. Phys. Chem. A XXXX, XXX, XXX−XXX

ones. The same observation applies at the XsTD-DFT level. As mentioned in the introduction, the sTD-DFT approach utilizes a special parametrization when considering RSH functionals but still solves Casida's equations for the GH case.[93] This parametrization was performed to reproduce reference excitation energies obtained at the SCS-CC2/def2-TZVP(-f).[93] For both QUEST and CT sets, the correlations between sCAM-B3LYP or sωB97X-D3 excitation energies with respect to RI-CC2 ones illustrate the suitability of these excellent parametrizations (Figures 9 and S6). For the QUEST set (see Table S3), we obtained MADs of 0.37 and 0.20 eV for sCAM-B3LYP and CAM-B3LYP, respectively, as well as MADs of 0.25 and 0.13 eV for the CT set (see Table S4).

Similar observations than for excitation energies can be done for oscillator strengths when changing DFAs with a few remarks: (i) when considering the QUEST set, for GH functionals with a low amount of HFX, XsTD-DFT oscillator strengths compare surprisingly better than TD-DFT ones with respect to RI-CC2 results. For class c_1, we obtain MADs as low as 0.010 (0.021) and 0.007 (0.016) for XsB3LYP (B3LYP) and XsPBE0 (PBE0), respectively. (ii) For GH functionals with a large amount of Fock exchange, large RI-CC2 oscillator strengths from the c_3 class are especially well reproduced by XsTD-DFT ones. For the QUEST set, MADs of 0.055 (0.125) and 0.131 (0.192) are obtained at the XsBHandHLYP (BHandHLYP) and XsM06-2X (M06-2X) levels of theory, respectively. For the CT set, considering RI-CC2 oscillator strengths $\in$[0.29,2.28], very low MADs of 0.07 and 0.09 are obtained at both XsBHandHLYP and BHandHLYP levels. (iii) For the CT set, the XsTD-DFT approach using RSH functionals provides oscillator strengths comparable to the RI-CC2 ones, with MADs of 0.10 and 0.14 for XsωB97X-D3 and XsωB97M-V, respectively, not far from TD-DFT ones of 0.08 and 0.13.

In general, when computing excited-state energies and oscillator strengths, the XsTD-DFT method clearly shows the same behavior as TD-DFT as a function of the amount of HFX with the GH DFA, a feature lost with the sTD-DFT scheme using the default parametrization. Table S6 reports the maximum absolute deviation (AD) for (X)sTD-DFT excitation energies from TD-DFT ones. For each DFA, considering both QUEST and CT sets, the XsTD-DFT scheme provides a smaller maximum AD than sTD-DFT with respect to TD-DFT. The only exceptions are for CT set excitation energies computed at XsTPSSH and XsωB97X-D3 levels of theory with 1.10 and 0.68 eV ADs larger than 0.92 and 0.19 eV at the sTD-DFT level. These results highlight the closeness between XsTD-DFT and TD-DFT results and illustrate the improvement over the former sTD-DFT scheme.

One of the known flaws of current simplified methods is the poor treatment of local $n \rightarrow \pi^*$ excitations as discussed in the introduction. Some transitions in our sets exhibit unambiguous $n \rightarrow \pi^*$ character. Table S7 reports excitation energies at the TBE/aug-cc-pVTZ, RI-CC2, TD-DFT, sTD-DFT, and XsTD-DFT levels of theory for such excitations. While RI-CC2 $\Delta E_{n\rightarrow\pi^*}$ follow TBE ones with a mean deviation (MD) of −0.004 eV, PBE0, sPBE0, and XsPBE0 exhibit MDs of −0.20 eV, −0.34 eV, and −0.43 eV, respectively. When increasing the amount of HFX in the functional, TD-DFT results present larger MDs with respect to TBE, with MD = 0.31 eV for BHandHLYP and MD = 0.07 eV for M06-2X. Interestingly, sBHandHLYP (MD = −0.02 eV) and XsBHandHLYP (MD = 0.10 eV) mostly improve over BHandHLYP, while sM06-2X (MD = −0.47 eV) and XsM06-2X (MD = −0.44 eV) globally underestimate TBE $\Delta E_{n\rightarrow\pi^*}$. Among RSH exchange−correlation functionals, CAM-B3LYP compares the best with respect to TBE, with MD = 0.05 eV, while ωB97X-D3 and ωB97M-V tend to overestimate TBE results, with MD values of 0.13 and 0.17 eV, respectively. We obtained MDs with respect to TBE excitation energies of −0.13 eV, −0.05 eV, and 0.00 eV at XsCAM-B3LYP, XsωB97X-D3, and XsωB97M-V levels, respectively. The XsTD-DFT results using RSH functionals systematically underestimate TD-DFT.

Figure S8 presents excitation energies for the first (S_1) and second (S_2) excited states of phthalazine computed at TD-DFT, sTD-DFT, and XsTD-DFT levels for PBE0, M06-2X, BHandHLYP, CAM-B3LYP, ωB97X-D3, and ωB97M-V functionals as well as for TBE and RI-CC2 levels. The dominant pairs of natural transition orbitals (NTOs) for both transitions computed at the XsPBE0 level of theory are also given and demonstrate their $n \rightarrow \pi^*$ character. As a function of the DFA employed, XsTD-DFT excitation energies systematically underestimate TD-DFT energies while closely following TD-DFT trends. For the transition to the S_1 state, XsTD-DFT excitation energies evaluated with XsCAM-B3LYP, XsωB97X-D3, and XsωB97M-V RSH DFAs are close to TBE values, with less than 0.1 eV of difference. This represents a systematic improvement with respect to the full scheme. It is either error compensations due to the approximation on two-electron integrals or the neglect of the exchange−correlation kernel that is responsible for this behavior with the XsTD-DFT scheme. To assess this further, Figure S8 also provides excitation energies computed with the XsTD-DFT scheme but using the canonical transformation of two-electron integrals from the AO space to the MO space (namely XsTD-DFT-full) only for GH DFAs. Restoring two-electron integrals in the XsTD-DFT scheme leads to excitation energies very near TD-DFT ones, showing that the neglect of the exchange−correlation kernel has little impact on these energies for this system. Thus, error compensations due to the approximation on two-electron integrals are probably responsible for this systematic improvement with respect to the full scheme. This observation suggests that understanding how errors propagate within the XsTD-DFT scheme with respect to the full scheme could give insights into how to improve it.

For both QUEST and CT sets, Figures S9 and S10 present correlation plots for the sTD-DFT-xTB excitation energies and oscillator strengths with respect to RI-CC2 ones, respectively. Table S8 provides the corresponding MADs and RMSDs. Excitation energies' MADs with respect to RI-CC2 ones are 0.47 and 0.16 eV for QUEST and CT sets, respectively. For the QUEST set, RI-CC2 excitation energies are almost systematically underestimated by the sTD-DFT-xTB method, and sTD-DFT-xTB results are significantly spread with respect to the reference with an RMSD of 0.56. The MAD of 0.47 eV is smaller than those for GH functionals with a large amount of HFX at the sTD-DFT level and of the same order of magnitude as the sωB97X-D3 one (MAD = 0.45 eV). All XsTD-DFT MADs are smaller than the sTD-DFT-xTB one (Table S8) for the QUEST set. For the CT set, sTD-DFT-xTB excitation energies present a small MAD of 0.16 eV with respect to RI-CC2 ones. As for the QUEST set, sTD-DFT-xTB excitation energies underestimate RI-CC2 ones, and results are spread according to an RMSD of 0.20 eV. The sTD-DFT-xTB scheme outperforms all sTD-DFT GH results for excitation energies with MADs $\geq$ 0.48 eV. The sTD-DFT-xTB MAD compares very well with the RSH sωB97X-D3 one of 0.15 eV. With respect to XsTD-DFT MADs, the sTD-DFT-xTB one of 0.16 eV is comparable to ones

https://doi.org/10.1021/acs.jpca.5c03189
J. Phys. Chem. A XXXX, XXX, XXX−XXX

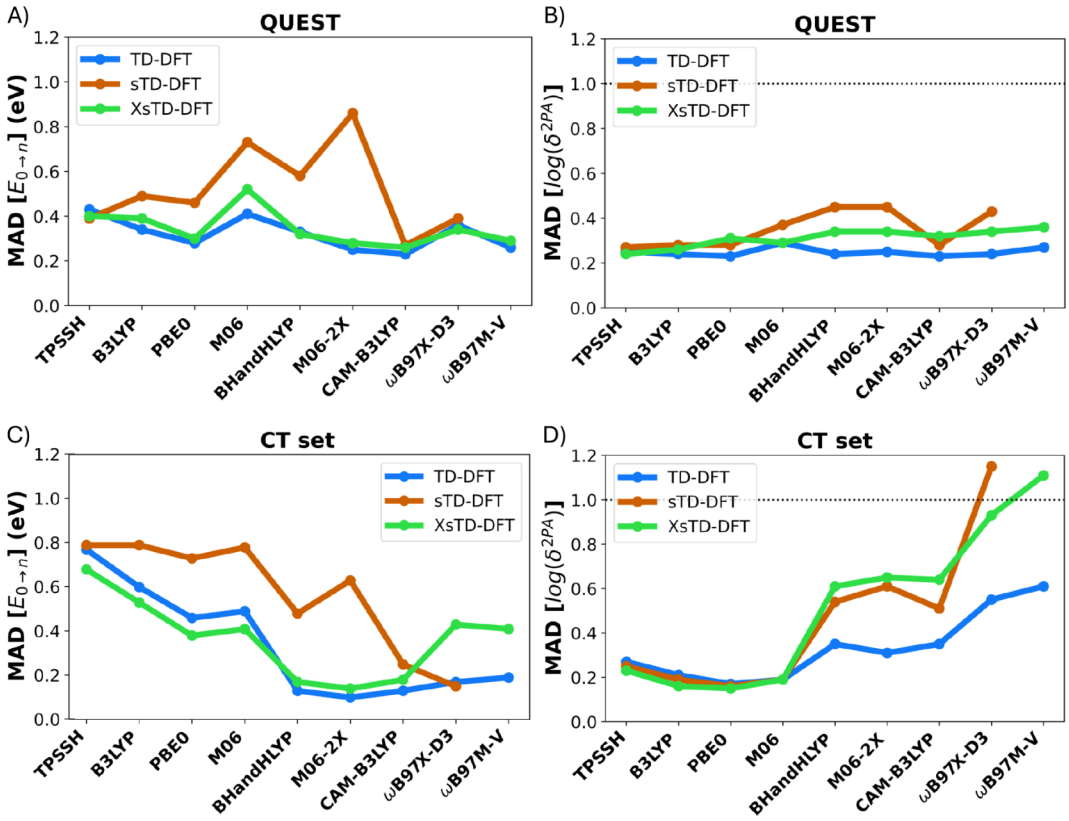

Figure 10. For both QUEST and CT sets, MADs for excitation energies as well as for $\log(\delta^{2PA})$ computed at TD-DFT, sTD-DFT, and XsTD-DFT levels of theory using TPSSH, B3LYP, PBE0, M06, BHandHLYP, M06-2X, CAM-B3LYP, ωB97X-D3, and ωB97M-V exchange−correlation functionals with respect to the RI-CC2 results using the aug-cc-pVDZ basis set.

at XsBHandHLYP (0.17 eV), XsM06-2X (0.14 eV), and XsCAM-B3LYP (0.18 eV) levels.

Regarding oscillator strengths, the sTD-DFT-xTB MAD of 0.08 with respect to RI-CC2 is much smaller than sTD-DFT ones (MAD > 0.09) but comparable to XsM06-2X (0.07), XsCAM-B3LYP (0.08), and XsωB97X-D3 (0.08) ones for the QUEST set. Larger oscillator strengths are better described (MAD c_3 = 0.05) than smaller ones (MAD c_1 = 0.04 and MAD c_2 = 0.10). Concerning CT excitations, the sTD-DFT-xTB oscillator strengths' MAD of 0.17 is larger than XsTD-DFT ones when using GH exchange-correlation functionals with a large amount of HFX (MADs $\leq$ 0.10) or RSH exchange−correlation functionals (MADs $\leq$ 0.14). Overall, sTD-DFT-xTB oscillator strengths correlate rather well with RI-CC2 ones (Figures S9 and S10), with a tendency to overestimate larger oscillator strengths from the CT set (Figure S10). sTD-DFT-xTB results correlate rather well with RI-CC2 ones even if excitation energies are more spread. We already discussed in the introduction the impossibility to directly connect the XsTD-DFT method with the usual xTB ground state. The present results motivate us to pursue this goal.

As intermediate conclusions for 1PA, the XsTD-DFT scheme is a *robust* and *reliable* method that exhibits a rather consistent behavior with respect to RI-CC2 results, similarly to TD-DFT upon varying the amount of HFX. In particular, XsBHandHLYP and XsM06-2X levels of theory are able to reproduce BHandHLYP and M06-2X results at a fraction of the computational cost (3 orders of magnitude in CPU time). In light of these findings, the XsTD-DFT method could be used as a *computationally efficient*, *reliable*, and *robust* alternative to TD-DFT to compute the 1PA spectra. The next section discusses if these requirements are still met for 2PA, which is more challenging to evaluate.

Two-Photon Absorption. For both QUEST and CT sets, Figure 10 presents MADs for excitation energies as well as for $\log(\delta^{2PA})$ computed at the TD-DFT, sTD-DFT, and XsTD-DFT levels of theory using TPSSH, B3LYP, PBE0, M06, BHandHLYP, M06-2X, CAM-B3LYP, ωB97X-D3, and ωB97M-V exchange−correlation functionals with respect to the RI-CC2 results. MAD values are collected in Tables S4 (CT set) and S9 (QUEST). For both sets, excitation energy and $\log(\delta^{2PA})$ correlation plots for TD-DFT, sTD-DFT, and XsTD-DFT methods with respect to RI-CC2 are displayed in Figures S11 (TPSSH), S12 (B3LYP), S13 (PBE0), S14 (M06), S15 (M06-2X), S16 (BHandHLYP), S17 (CAM-B3LYP), S18 (ωB97X-D3), and S19 (ωB97M-V). MADs for 2PA strengths are reported considering $\log(\delta^{2PA})$ because the range of δ^{2PA} across both sets of molecules spans from very small 2PA strengths around 1 a.u. to values as large as 10^6 a.u. For both sets, excitation energy MAD trends for TD-DFT, sTD-DFT, and XsTD-DFT schemes with respect to the RI-CC2 method considering 2P-active states are the same as those already discussed for 1P-active ones. Correlation plots are also similar (see Figures S11−S19). DFAs with a small amount of HFX provide XsTD-DFT and TD-DFT $\log(\delta^{2PA})$ that correlate well with respect to RI-CC2 ones. Using the B3LYP functional, for the QUEST set, MADs of 0.28, 0.26, and 0.24 are obtained for sTD-DFT, XsTD-DFT, and TD-DFT levels, respectively. This corresponds to an absolute deviation from RI-CC2 of less than 1/3 order of magnitude. For the CT set, even smaller MADs are obtained with PBE0: 0.16, 0.15, and 0.17 for sTD-DFT, XsTD-DFT, and TD-DFT levels, respectively. Note that while MADs

https://doi.org/10.1021/acs.jpca.5c03189
J. Phys. Chem. A XXXX, XXX, XXX−XXX

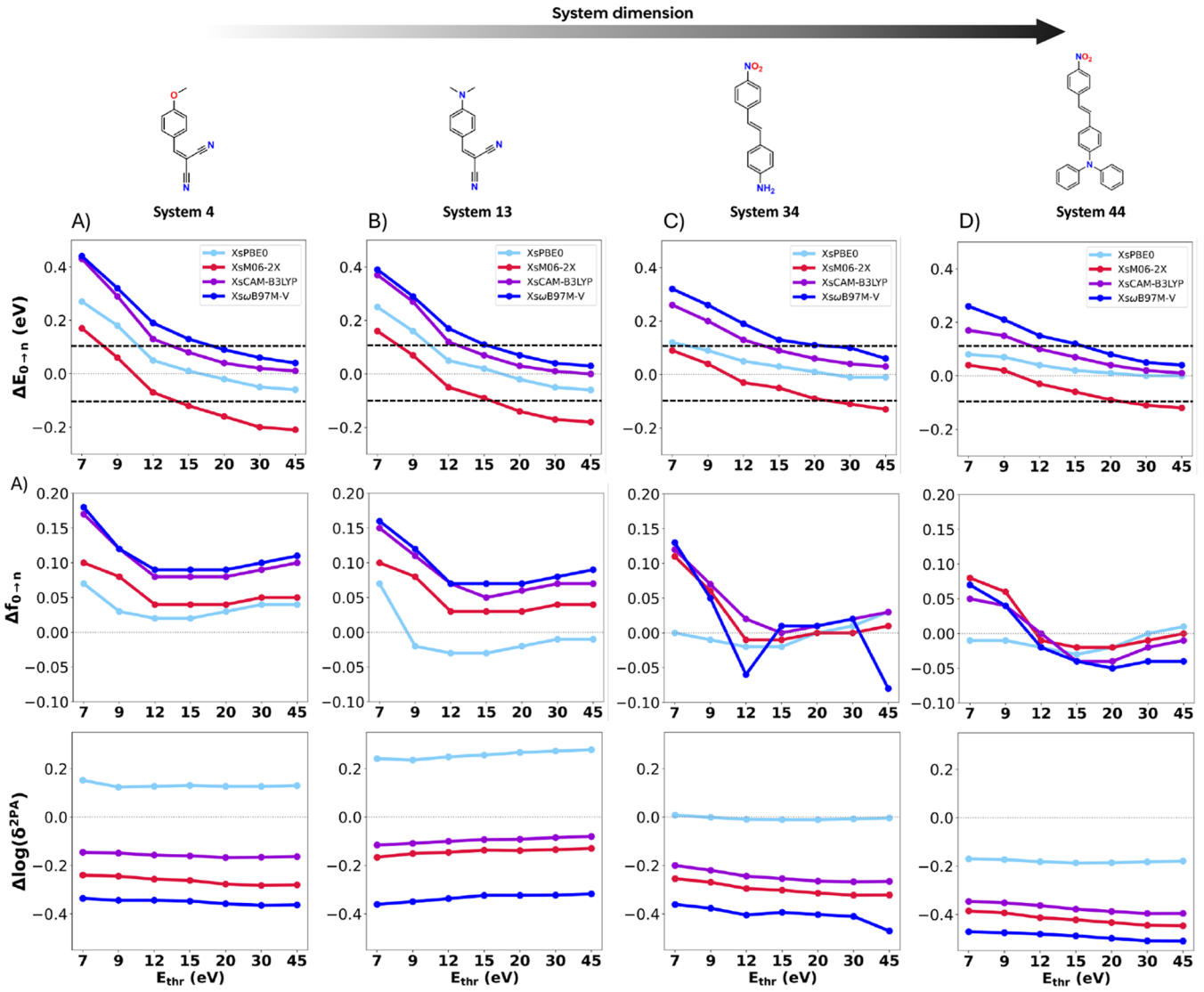

[4]	$E_{0\to n}$	$f_{0\to n}$	$log(\delta^{2PA})$
PBE0	3.85	0.79	3.24
M06-2X	4.06	0.82	3.29
CAM-B3LYP	4.01	0.82	3.25
ωB97M-V	4.09	0.82	3.24

[13]	$E_{0\to n}$	$f_{0\to n}$	$log(\delta^{2PA})$
PBE0	3.47	0.85	3.57
M06-2X	3.66	0.92	3.67
CAM-B3LYP	3.64	0.92	3.61
ωB97M-V	3.73	0.93	3.62

[34]	$E_{0\to n}$	$f_{0\to n}$	$log(\delta^{2PA})$
PBE0	3.00	0.87	4.74
M06-2X	3.49	1.14	4.46
CAM-B3LYP	3.45	1.15	4.44
ωB97M-V	3.68	1.20	4.17

[44]	$E_{0\to n}$	$f_{0\to n}$	$log(\delta^{2PA})$
PBE0	2.62	0.86	5.26
M06-2X	3.22	1.29	4.85
CAM-B3LYP	3.22	1.34	4.81
ωB97M-V	3.49	1.45	4.46

Figure 11. For systems 4, 13, 34, and 44 from the CT set, XsTD-DFT excitation energies, oscillator strengths, and $\log(\delta^{2PA})$ deviations from TD-DFT results as a function of E_{thr} for PBE0, M06-2X, CAM-B3LYP, and ωB97M-V exchange−correlation functionals with the aug-cc-pVDZ basis set. Tables at the bottom show TD-DFT excitation energies, oscillator strengths, and $\log(\delta^{2PA})$ for each system.

for $\log(\delta^{2PA})$ are similar to both sTD-DFT and XsTD-DFT methods, excitation energies are better reproduced by the XsTD-DFT method with a MAD of only 0.38 eV instead of 0.73 eV with the sTD-DFT method. We already showed that increasing the amount of HFX in the functional decreases MADs on excitation energies with respect to RI-CC2 values for TD-DFT and XsTD-DFT schemes, while sTD-DFT results are poor. This is not the case when considering $\log(\delta^{2PA})$. Going from B3LYP to BHandHLYP, for the QUEST set, the MAD increases from 0.26 to 0.34 and from 0.16 to 0.61 for the CT set at the XsTD-DFT level. Correlation plots for M06-2X and BHandHLYP functionals (Figures S15 and S16) illustrate a systematic underestimation of the reference values, especially for the larger 2PA strengths from the CT set. For the QUEST set, XsBHandHLYP (BHandHLYP) and XsM06-2X (M06-2X) levels better correlate with RI-CC2 results with MADs of 0.34 (0.24) and 0.34 (0.25), respectively. Similar trends than for GH functionals with a large amount of HFX are observed considering RSH functionals. For the QUEST set, rather good performances are obtained for XsCAM-B3LYP and sCAM-B3LYP levels with MADs of 0.32 and 0.28 with respect to RI-CC2 results, not far from the CAM-B3LYP MAD of 0.23. For the CT set, XsTD-DFT and sTD-DFT levels systematically underestimate RI-CC2 $\log(\delta^{2PA})$ when using RSH functionals, while MADs are more contained for the full scheme. These discrepancies with simplified methods are probably related to neglect to the response of the exchange−correlation kernel in the evaluation of the single residue of the quadratic functions,

https://doi.org/10.1021/acs.jpca.5c03189
J. Phys. Chem. A XXXX, XXX, XXX−XXX

especially for GH functionals with a large amount of HFX as well as RSH DFAs. We are currently investigating this issue. MADs of $\log(\delta^{2PA})$ computed with sTD-DFT and XsTD-DFT levels remain comparable, but MADs for excitation energies are lower with the XsTD-DFT method.

Computing 2PA cross sections with the XsTD-DFT method requires the same considerations in terms of the choice of DFA as for the full TD-DFT scheme. On one hand, GH DFAs with a lower amount of HFX better capture δ^{2PA} with respect to RI-CC2 ones. On the other hand, computing excitation energies comparable to RI-CC2 ones requires a larger amount of HFX in the GH DFAs or RSH DFAs. To compute 2PA spectra with either TD-DFT or XsTD-DFT methods, we propose to use PBE0 or B3LYP DFAs as a compromise to better reproduce RI-CC2 excitation energies and δ^{2PA}. These observations are consistent with previous studies[33,34] that benchmarked 2PA evaluated with the TD-DFT method with respect to the RI-CC2 one. Chołuj et al.[33] showed that the TD-DFT scheme using RSH DFAs severely underestimates 2PA strengths, while GH functionals better reproduce absolute 2PA strengths for many CT set donor−acceptor molecules. These conclusions are also valid for the XsTD-DFT method as shown here.

For both QUEST and CT sets, Figures S9 and S10 present correlation plots for the sTD-DFT-xTB $\log(\delta^{2PA})$ with respect to the RI-CC2 ones, respectively. Table S8 provides corresponding MADs and RMSDs. As we did for 1PA, we now discuss the performance of sTD-DFT-xTB to compute 2PA strengths for both the QUEST and CT sets. For the QUEST set, the sTD-DFT-xTB $\log(\delta^{2PA})$ MAD of 0.40 with respect to RI-CC2 reference values is larger than all sTD-DFT and XsTD-DFT results, with the exception of sBHandHLYP, sM06-2X, and sωB97X-D3 ones. For the CT set, the MAD remains on the same order of magnitude, with a value of 0.45 with respect to the RI-CC2 reference $\log(\delta^{2PA})$. Only sTD-DFT and XsTD-DFT results obtained using GH functionals with a small amount of HFX present smaller MADs. Nonetheless, the sTD-DFT-xTB method has already provided 2PA spectra that compare very well with respect to experiments for bacteriorhodopsin, iLOV, and the FMN in aqueous solution.[74,76]

In summary, the same considerations regarding the choice of DFAs in TD-DFT apply to compute the 2PA with the XsTD-DFT method. In particular, the XsPBE0 level of theory offers a good compromise between reproducing RI-CC2 peak positions (i.e., excitation energies) and 2PA intensities (i.e., 2PA strengths), especially for excited states from the CT set that are common 2P-active dyes. This recommendation is solely based on calculations for molecules in a vacuum and should be viewed as an initial guideline when comparing theory to experiment. This highlights the need to extend the present study to microsolvated systems to understand how the XsTD-DFT method captures the impact of noncovalent interactions on 1PA and 2PA. This will be addressed in a following section. We will also examine how single-molecule XsTD-DFT 1PA and 2PA calculations compare to the experimental data.

Basis Set Effects. The two previous sections mostly discussed the impact of the DFA on the computation of 1 and 2PA with TD-DFT, sTD-DFT, and XsTD-DFT schemes with respect to RI-CC2 reference calculations using the aug-cc-pVDZ basis set. Basis set effects are now briefly discussed focusing on PBE0, CAM-B3LYP, and ωB97X-D3 DFAs, considering 3-21G(d), 6-31G(d), cc-pVDZ, def2-SVP, 6-31+G(d), and aug-cc-pVDZ basis sets. For a detailed discussion, the reader is encouraged to read the Supporting Information where basis set effects are discussed for both the CT set (Figure S20) and QUEST set (Figure S21). Note that for sTD-DFT calculations, basis set effects are only accounted for in the evaluation of two-electron integrals by the Löwdin-orthogonalized LCAO coefficients (eq 1) because of the collection of Löwdin-orthogonalized two-electron integrals (eq 2) approximated by the MNOK damped Coulomb operator (eqs 3 and 4) that has no basis set dependence. One of the main ideas behind developing the XsTD-DFT scheme was to recover this basis set dependence by approximating Löwdin-orthogonalized two-electron integrals by AO integrals.[3,73,92] Our results (Figures S20−S23) show that trends for both 1PA and 2PA properties computed with the XsTD-DFT method closely follow those calculated with TD-DFT across different basis sets. As expected, the largest basis sets investigated here (i.e., 6-31+G(d) and aug-cc-pVDZ) are recommended to compute excitation energies and δ^{2PA} with the XsTD-DFT scheme. Oscillator strengths appear to be less dependent on the basis set size. The choice of the DFA has a larger impact on XsTD-DFT results than the selection of a double-ζ basis set compared to RI-CC2/aug-cc-pVDZ results. Beyond the choice of the DFA and basis set, an important method-specific input parameter that impacts XsTD-DFT results is the selection of the energy threshold used to truncate the CIS space. The following section examines the influence of E_{thr} on 1PA and 2PA properties computed with the XsTD-DFT scheme.

Impact of the Truncation of the CIS Space on XsTD-DFT Results. Figure 11 presents, for molecules 4, 13, 34, and 44 of the CT set, XsTD-DFT excitation energies, oscillator strengths, and $\log(\delta^{2PA})$ deviations from TD-DFT results as a function of E_{thr} for PBE0, M06-2X, CAM-B3LYP, and ωB97M-V exchange−correlation functionals. Systems 4 and 13 were selected because their XsPBE0 δ^{2PA} of 2324 and 6452 a.u. considering E_{thr} = 9 eV diverge strongly from RI-CC2 reference values of 7868 and 18758 au. Systems 34 and 44 were selected, and they have XsPBE0 δ^{2PA} of 55174 and 122005 a.u. that are in excellent agreement with RI-CC2 values of 51408 and 150580 au. As mentioned in the introduction, E_{thr} in the sTD-DFT and XsTD-DFT methodologies selects relevant CSFs for the range of excitation energies considered. Technically, the primary CSF space (P-CSF) is selected by evaluating $A_{ia,ia} \leq E_{thr}$ and the secondary CSF space (S-CSF) by second-order perturbative expressions using $A_{ia,jb}$ elements that could couple primary CSFs to a higher-energy $j \rightarrow b$ one. The spaces of selected CSFs are the sum of both primary and secondary CSFs.

Considering excitation energies for the four systems, XsCAM-B3LYP and XsωB97M-V deviations with respect to TD-DFT results slowly decrease as a function of E_{thr}. This behavior is symptomatic of a slower convergence of XsTD-DFT excitation energies toward TD-DFT ones when using RSH and might explain the large MADs we obtained for XsωB97M-V (0.41 eV) and XsωB97X-D3 (0.43 eV) with respect to the RI-CC2 level when using E_{thr} = 9 eV (see Figure S24). For the CT set, when computing excitation energy MADs with a larger energy threshold of 20 eV, we observe a substantial improvement for both the XsωB97M-V (0.28 eV) and XsωB97X-D3 (0.30 eV) levels. Excitation energies computed at the XsM06-2X level start to diverge from M06-2X ones when E_{thr} is larger than ∼9 to 12 eV. The same behavior is observed for XsPBE0 considering systems 4 and 13 for E_{thr}> 12 eV. Thus, an E_{thr} sweet spot exists for which the XsTD-DFT excitation energies converge toward the TD-DFT ones when using GH DFAs. For these four systems, the E_{thr} value required to compute XsTD-DFT

https://doi.org/10.1021/acs.jpca.5c03189
J. Phys. Chem. A XXXX, XXX, XXX−XXX

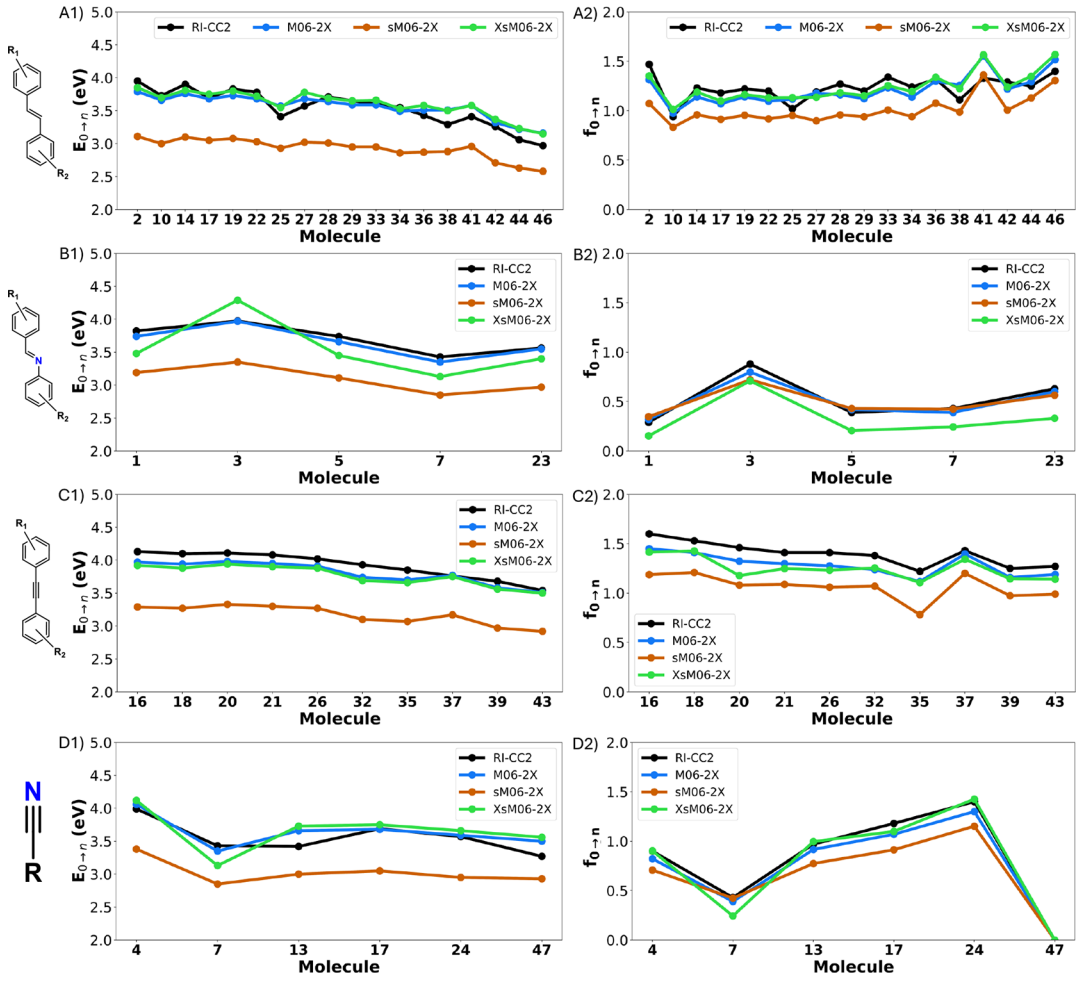

Figure 12. For subsets from the CT set of substituted stilbene, para-substituted benzalanine, and substituted bisphenylacetylene molecules as well as compounds with cyanide groups, excitation energies, and oscillator strengths computed at RI-CC2, M06-2X, sM06-2X, and XsM06-2X levels of theory using the aug-cc-pVDZ basis set.

excitation energy deviations in the interval $[-0.1, 0.1]$ eV seems to decrease upon increasing the size of the molecule.

Deviations of XsTD-DFT oscillator strengths from TD-DFT ones remain between −0.10 and 0.20 within the range of E_{thr}. Considering that TD-DFT oscillator strengths for these systems are between 0.79 and 1.45, XsTD-DFT errors with respect to TD-DFT results are rather small. For most of DFAs, we observe an overall convergence of XsTD-DFT oscillator strengths toward TD-DFT ones as E_{thr} increases, with a tendency to reach a slowly diverging plateau for E_{thr} values larger than 12−15 eV, except for system 34 at the XsωB97M-V level.

For these four systems, XsTD-DFT $\log(\delta^{2PA})$ absolute deviations do not show any clear convergence with respect to the TD-DFT results as a function of E_{thr}. Depending on the system and the DFA used, trends can slightly diverge or slowly converge as a function of E_{thr}.

Figure S25 shows for molecules 4, 13, and 34 of the CT set XsTD-DFT excitation energies, oscillator strengths, and $\log(\delta^{2PA})$ deviations from TD-DFT results as a function of E_{thr} for PBE0 and M06-2X. For comparison, Figure S25 also includes deviations computed with the XsTD-DFT scheme but using the canonical transformation of two-electron integrals from the AO space to the MO space (XsTD-DFT-full) instead of the ZDO approximation. The development version of `std2` can compute the four-index transformation from the AO to the MO space. This implementation is not optimized and was only for testing purposes during the development process. Therefore, we were able to obtain XsTD-DFT-full results for only a few systems and E_{thr} values. While the response of the exchange−correlation kernel is still neglected in the XsTD-DFT-full methods, results clearly show a rather similar convergence as the XsTD-DFT method. This is an indication that a TD-DFT method using the same E_{thr} procedure could behave similarly to the XsTD-DFT method. For the investigated systems, we observe a systematic shift of excitation energies passing from the XsTD-DFT scheme to the XsTD-DFT-full one. The slower convergence of the XsTD-DFT-full excitation energy with respect to the final TD-DFT value as a function of E_{thr} highlights one possible source of error compensation in TD-DFT between the exchange−correlation kernel (absent in XsTD-DFT) and the contribution of canonical two-electron integrals. Consequently, reintroducing these integrals into the kernel-free XsTD-DFT method could require a larger number of CSFs (i.e., a large E_{thr} value) to reproduce TD-DFT excitation energies.

Figure S26 presents XsPBE0/aug-cc-pVDZ 2PA calculation CPU times computed on 16 CPU (Intel Xeon E5-2650 v2, 2.60 GHz) computer nodes as well as numbers of CSFs, P-CSFs, and S-CSFs included in as a function *of* E_{thr} for systems 4, 13, 34, and 44 of the CT set. Employing E_{thr} larger than 15 eV drastically increases computational timings for XsTD-DFT calculations

https://doi.org/10.1021/acs.jpca.5c03189
J. Phys. Chem. A XXXX, XXX, XXX−XXX

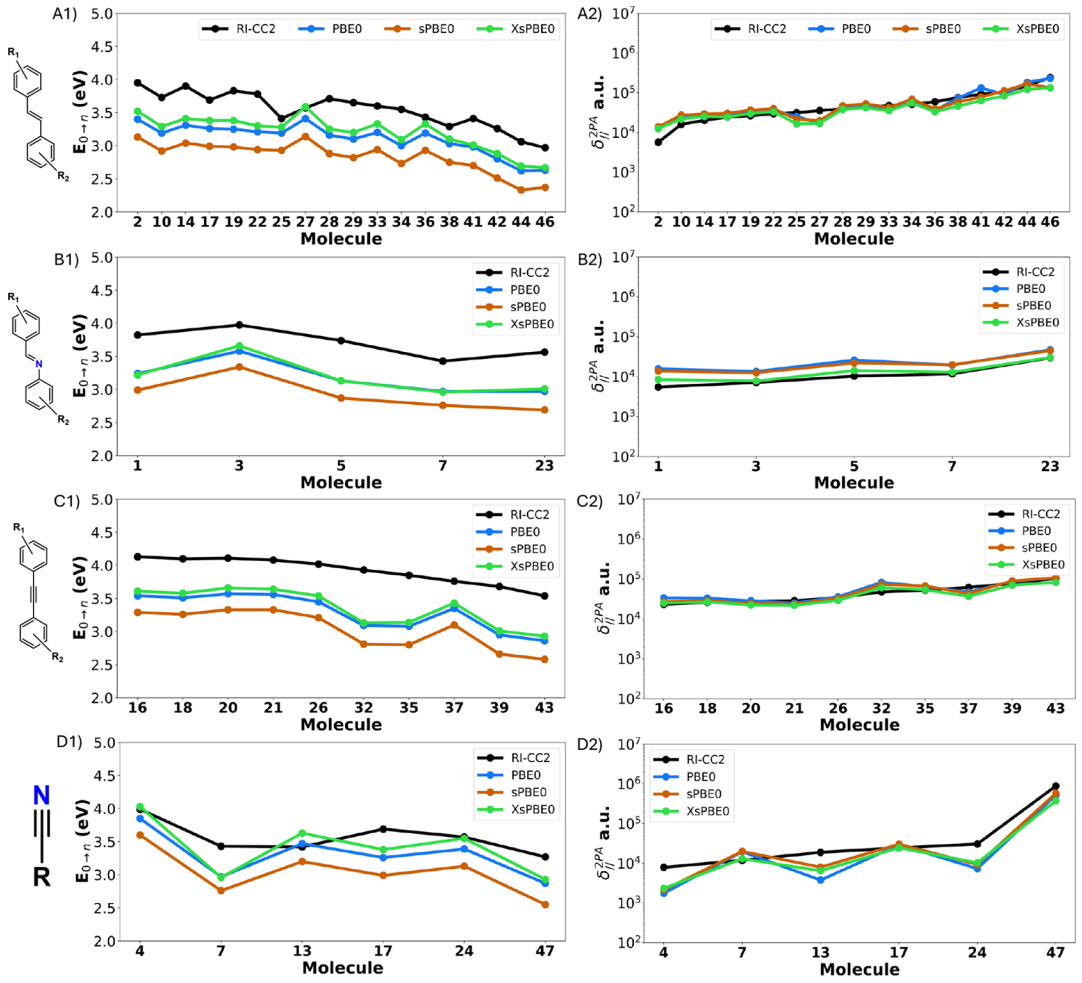

Figure 13. For subsets from the CT set of substituted stilbene, para-substituted benzalanine, and substituted bisphenylacetylene molecules, as well as compounds with cyanide groups, excitation energies, and 2PA strengths computed at RI-CC2, PBE0, sPBE0, and XsPBE0 levels of theory using the aug-cc-pVDZ basis set.

with the `std2`[101] program, while results are not necessarily improved with respect to the full scheme as we discussed above. For example, the CPU time required to compute up to 8628 excited states and 20 2PA strengths for system 44 was below 7 h with $E_{thr} \leq 20$ eV and about 126 h for $E_{thr} = 45$ eV (30642 excited states and 20 2PA strengths). As E_{thr} increases, the dimensionality of the P-CSF space expands as anticipated, but the S-CSF space reaches a peak beyond which a progressively smaller number of S-CSFs is incorporated into the CSF space.

In summary, for the four compounds selected from the CT set, we observe that deviations of the XsTD-DFT excitation energies from the TD-DFT values decrease monotonically with the energy threshold. Because of this, one can identify an optimal E_{thr} value that yields excitation energies close to TD-DFT ones. For XsPBE0 and XsM06-2X levels, selecting $E_{thr} \in [9, 12]$ eV results in deviations from PBE0 and M06-2X excitation energies of less than 0.1 eV. When using RSH functionals such as CAM-B3LYP and ωB97M-V, the convergence of XsTD-DFT excitation energies toward TD-DFT values occurs at larger energy thresholds. When selecting an appropriate E_{thr} value to compute 1PA and 2PA, one should select the smallest value to ensure convergence and minimize the number of CSFs, keeping the method *computationally efficient* and *reliable*. This consideration is particularly important given the steep scaling of the XsTD-DFT method (Figure S26).

Structure−Property Relationships. Trends among different chemical structures for excitation energies, oscillator strengths, and 2PA strengths are investigated to assess the robustness of simplified methods. From the CT set, four subsets of compounds were identified: substituted stilbene (2, 10, 14, 17, 19, 22, 25, 27−29, 33, 34, 36, 38, 41, 42, 44, and 46), para-substituted benzalanine (1, 2, 5, 7, and 23), and substituted bisphenylacetylene (16, 18, 20, 21, 26, 32, 35, 37, 39, and 43) molecules, as well as compounds with cyanide groups (4, 7, 13, 17, 24, and 47). For the CT set, the XsM06-2X level of theory provides excitation energies and oscillator strengths that compare very well with RI-CC2 reference calculations, with an excitation energy MAD of 0.14 eV and an oscillator strength MAD of 0.10. Thus, the M06-2X exchange−correlation functional was selected to discuss structure−property relationships among subsets of compounds for 1PA properties. For each subset, Figure 12 presents excitation energies and oscillator strengths computed at RI-CC2, M06-2X, sM06-2X, and XsM06-2X levels of theory. For each subset, XsM06-2X excitation energies closely follow M06-2X ones except for substituted benzalanine molecules where larger deviations are observed while keeping the same trend. RI-CC2 trends among compounds are not fully followed by the TD-DFT ones. sTD-DFT excitation energies are globally underestimated with respect to TD-DFT ones. Similar observations can be made

https://doi.org/10.1021/acs.jpca.5c03189
J. Phys. Chem. A XXXX, XXX, XXX−XXX

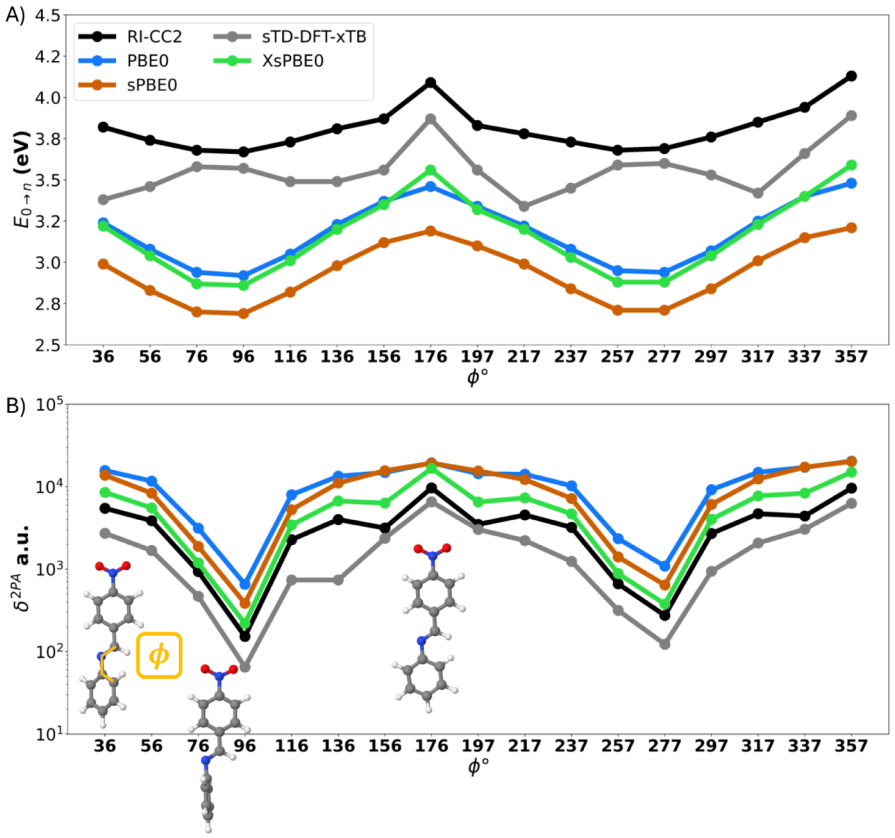

Figure 14. For system 1, rigid scans for excitation energies and 2PA strengths computed at RI-CC2, PBE0, sPBE0, XsPBE0, and sTD-DFT-xTB levels of theory as a function of the dihedral angle ϕ (highlighted in yellow).

for oscillator strengths. XsM06-2X slightly underestimates RI-CC2 oscillator strengths for benzalanine systems but consistently follows RI-CC2 trends. Among these subsets of molecules, XsM06-2X results present the same reliability as M06-2X ones, illustrating the *robustness* of the XsTD-DFT method to compute 1PA properties while remaining *computationally efficient*.

The XsPBE0 scheme provides the smallest $\log(\delta^{2PA})$ MAD of 0.15 with respect to RI-CC2 results among the set of DFAs considered in this study for the CT set. Note that the XsPBE0 excitation energy MAD is 0.38 eV with respect to the reference. For each subset, Figure 13 presents excitation energies and 2PA strengths computed at RI-CC2, PBE0, sPBE0, and XsPBE0 levels of theory. The analysis is straightforward, as XsPBE0 results closely follow PBE0 ones. sTD-DFT systematically underestimates TD-DFT excitation energies. RI-CC2 trends are not fully reproduced by TD-DFT especially for substituted stilbene, but results remain reasonable. For the subset of compounds with cyanide groups, RI-CC2 trends are not well followed by the other methods. Let us stress that XsPBE0 2PA strengths took only a few minutes to be computed. The improvement over δ^{2PA} when computed with the full scheme is rather marginal, but the extra computational cost to be paid is certainly not negligible. The results illustrate, at least when using the PBE0 exchange−correlation functional, the *robustness* of the XsTD-DFT method with respect to the full scheme to compute 2PA strengths at a fraction of the computational cost.

Among the subset of substituted stilbene molecules, compounds with an *N*,*N*-diphenylamine group, i.e., 25, 38, 41, 44, and 46, present larger δ^{2PA} deviations at the XsPBE0 level with respect to the full scheme. Their geometries are not planar because of this substituent. Analyzing the data for the entire CT set, we observe that XsPBE0 2PA strengths deviate more from PBE0 strengths for systems having their π-conjugated pathway distorted from planarity. To better understand this behavior, we performed a rigid scan varying the dihedral angle ϕ between the phenyl group and the rest of the π-conjugated pathway of compound 1 by step of $\Delta\phi = 20°$. At the equilibrium geometry, the dihedral angle is 36°. Figure 14 and Table S10 present rigid scans for excitation energies and 2PA strengths computed at the RI-CC2, PBE0, sPBE0, XsPBE0, and sTD-DFT-xTB levels of theory as a function of ϕ. XsPBE0 excitation energies almost perfectly reproduce PBE0 ones. Even if XsPBE0, sPBE0, and PBE0 trends follow the RI-CC2 one, these methods systematically underestimate RI-CC2 excitation energies, especially at the sPBE0 level. While sTD-DFT-xTB excitation energies are closer to RI-CC2 values, the RI-CC2 trend as a function of the dihedral angle is not well followed by sTD-DFT-xTB results. This is probably due to the xTB ground state for which diffuse functions are added non-self-consistently at the final step of the ground-state calculation.[78] 2PA results are more surprising as the XsTD-DFT method better reproduces RI-CC2 δ^{2PA} profile as a function of the dihedral angle for compound 1. sTD-DFT and TD-DFT results systematically provide larger δ^{2PA} with respect to RI-CC2 values. For the most planar geometries (e.g., ϕ = 176°), XsPBE0 δ^{2PA} are closer to PBE0 values, but for more distorted geometries (e.g., ϕ = 96°), they are closer to RI-CC2 ones. sTD-DFT-xTB δ^{2PA} values underestimate RI-CC2 values, and the RI-CC2 trend is not particularly well followed.

This section addressed two key questions from the introduction on the ability of the XsTD-DFT method to capture trends in optical properties with geometrical changes in

https://doi.org/10.1021/acs.jpca.5c03189
J. Phys. Chem. A XXXX, XXX, XXX−XXX

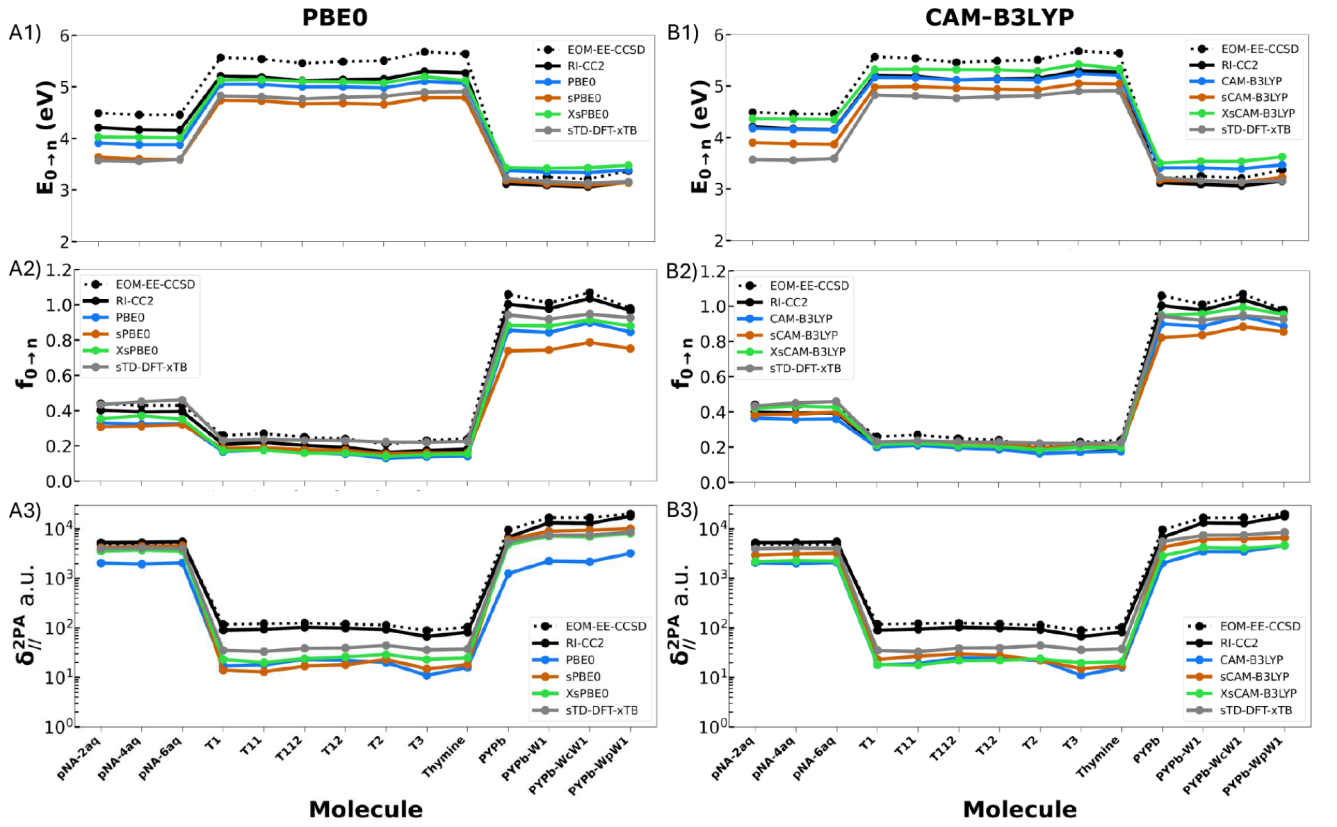

Figure 15. For microhydrated clusters, EOM-EE-CCSD/6-31+G(d) excitation energies, oscillator strengths, and δ^{2PA} (logarithmic scale)[69] as well as RI-CC2, TD-DFT, sTD-DFT, XsTD-DFT, and sTD-DFT-xTB ones using the aug-cc-pVDZ basis set. The left panel reports PBE0 results, while the right one considers CAM-B3LYP DFA.

comparison to both TD-DFT and RI-CC2 schemes as well as on the performance of the XsTD-DFT for nonequilibrium geometries, assessing the *robustness* and *reliability* of the method. Among the tested DFAs, the XsM06-2X and XsPBE0 levels of theory consistently reproduce TD-DFT trends for excitation energies, oscillator strengths, and 2PA strengths for four subsets of molecules extracted from the CT set. Varying the dihedral angle of compound 1, XsPBE0 results closely follow PBE0 ones for excitation energies and 2PA strengths, illustrating the *reliability* of the XsTD-DFT method for nonequilibrium geometries, a crucial feature for ADQM procedures. The next section will assess another important feature for such methodologies: how the XsTD-DFT captures optical properties for noncovalent interacting systems, such as microsolvated chromophores.

Microhydrated Systems. Simplified schemes are specifically designed to treat large systems, e.g., explicitly solvated chromophores used as realistic systems for AQM methodologies.[74] Thus, it is very important to assess the performance of such methods when dealing with microsolvation effects. For this scope, systems from Nanda and Krylov[69] were selected for which EOM-EE-CCSD/6-31+G(d) reference excitation energies, oscillator strengths, and 2PA strengths are available. Figure S27 displays MADs for excitation energies, oscillator strengths, and $\log(\delta^{2PA})$ computed at the TD-DFT, sTD-DFT, XsTD-DFT, and RI-CC2 levels of theory using B3LYP, PBE0, CAM-B3LYP, ωB97X-D3, and ωB97M-V exchange−correlation functionals as well as the aug-cc-pVDZ basis set with respect to EOM-EE-CCSD/6-31+G(d) reference calculations. Note that because we used the slightly larger aug-cc-pVDZ basis set for our calculations, the EOM-EE-CCSD/6-31+G(d) reference values from Nanda and Krylov[69] could introduce extra discrepancies. For transition energies, TD-DFT MADs among the set of DFAs are closely followed by XsTD-DFT MADs with respect to the EOM-EE-CCSD results. Excitation energy MADs are much larger with the sTD-DFT method. Using RSH exchange−correlation functionals, TD-DFT and XsTD-DFT MADs are similar to the RI-CC2 one of 0.28 eV with respect to the reference. For the whole range of DFAs, XsTD-DFT MADs are smaller than TD-DFT ones. Considering oscillator strengths, XsTD-DFT MADs with respect to EOM-EE-CCSD results also follow TD-DFT ones. XsCAM-B3LYP and XsωB97X-D3 levels both provide MADs of 0.04 exactly as the RI-CC2 one with respect to the reference. Here again, XsTD-DFT MADs are lower than TD-DFT MADs among the set of DFAs. Regarding 2PA strengths, TD-DFT MADs are large with respect to EOM-EE-CCSD results. XsTD-DFT MADs closely follow TD-DFT ones for RSH functionals but are much smaller using GH DFAs. Overall, XsTD-DFT results are closer to EOM-EE-CCSD ones than TD-DFT. This is an unexpected behavior for which we do not have a clear explanation at the moment.

For microhydrated clusters, Figure 15 reports EOM-EE-CCSD/6-31+G(d) excitation energies, oscillator strengths, and δ^{2PA} as well as RI-CC2, TD-DFT, sTD-DFT, XsTD-DFT, and sTD-DFT-xTB excitation energies using the aug-cc-pVDZ basis set. Displayed TD-DFT, sTD-DFT, and XsTD-DFT results were obtained with both PBE0 and CAM-B3LYP DFAs. Considering PBE0, XsTD-DFT excitation energies are the nearest to EOM-EE-CCSD ones, except for PYPb microhydrated clusters, for which the full scheme is slightly better.

https://doi.org/10.1021/acs.jpca.5c03189
J. Phys. Chem. A XXXX, XXX, XXX−XXX

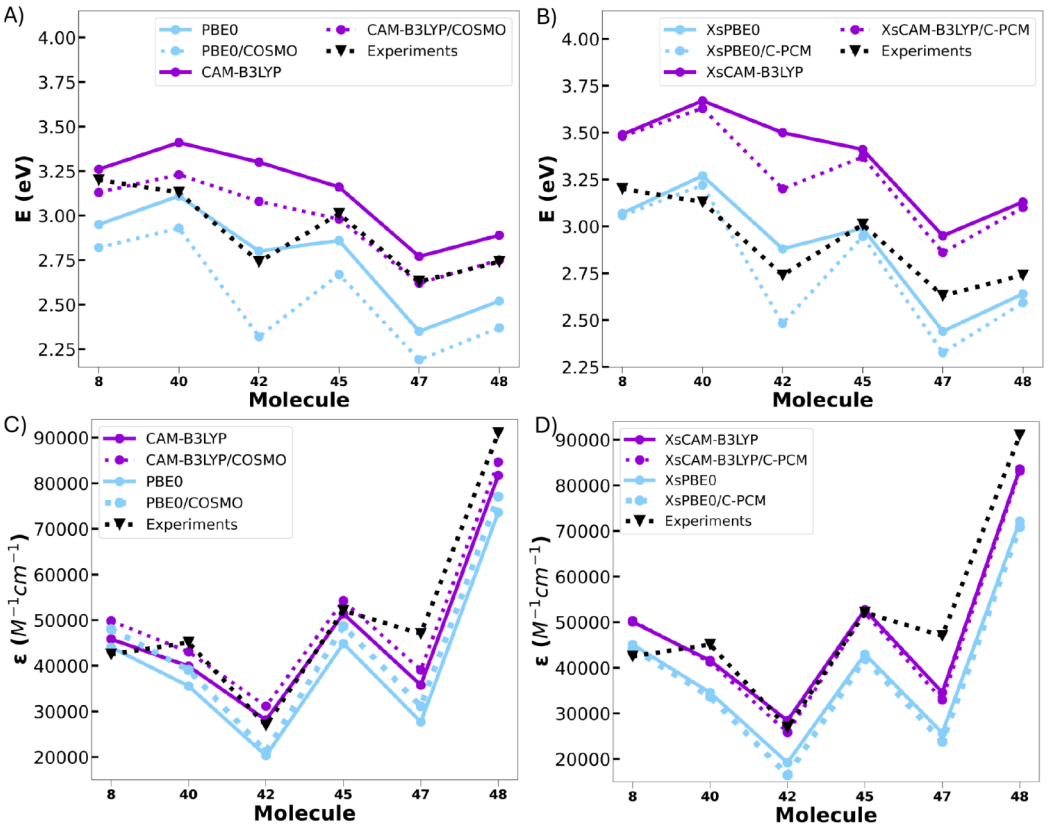

Figure 16. Experimental excitation energies and molar absorption coefficients (ε in M^{-1} cm^{-1}) for the absorption maximum of compounds 8, 40, 45, 47, and 48 recorded in toluene[108,109] and for compound 42 recorded in DMSO[110] in comparison with TD-DFT and XsTD-DFT theoretical ones in vacuum as well as TD-DFT/COSMO and XsTD-DFT/C-PCM. An empirical damping factor of 0.2 eV was used to compute molar absorption coefficients.

Both XsTD-DFT and TD-DFT schemes provide excitation energies close to RI-CC2 ones, except for PYPb clusters. Using the CAM-B3LYP DFA improves the comparison of XsTD-DFT results with respect to EOM-EE-CCSD ones for pNA and thymine families of microhydrated clusters. Except for the PYPb family of clusters, sTD-DFT and sTD-DFT-xTB methods provide excitation energies largely smaller than references.

Regarding oscillator strengths, XsTD-DFT and TD-DFT methods compare well to both RI-CC2 and EOM-EE-CCSD methods, especially by using the CAM-B3LYP exchange−correlation functional. XsCAM-B3LYP results outperform CAM-B3LYP ones with respect to EOM-EE-CCSD calculations. The best oscillator strengths are surprisingly obtained at the sTD-DFT-xTB level with respect to the reference, except the PYPb family, for which the XsCAM-B3LYP level provides better ones. EOM-EE-CCSD trends are relatively well followed by all of the schemes.

For pNA and PYPb families of mycrohydrated clusters, the EOM-EE-CCSD 2PA strengths are rather well reproduced by all simplified schemes using PBE0, outperforming the full scheme. For the thymine family, XsPBE0 provides the best comparison with respect to the EOM-EE-CCSD level. Using CAM-B3LYP worsens the results for simplified schemes with respect to reference calculations. Surprisingly, sTD-DFT-xTB 2PA strengths compare very well to the EOM-EE-CCSD strengths for the whole set of microhydrated systems. The sTD-DFT-xTB scheme already showed its suitability to be used in AQM approaches to reproduce experimental 2PA spectra.[74] Considering these systems, the literature provided 2PA strengths using different embedding schemes, including the CAM-B3LYP*/PDE-X level, using the extended polarizable density embedding model PDE-X, as well as the EOM-EE-CCSD/EFP level that uses the effective fragment potential approach. For all microhydrated clusters, Figure S28 presents EOM-EE-CCSD/6-31+G(d) δ^{2PA} (log scale)[69] as well as EOM-EE-CCSD/EFP,[69] CAM-B3LYP*/PDE-X,[97] and XsCAM-B3LYP ones. EOM-EE-CCSD/EFP 2PA strengths compare almost perfectly to EOM-EE-CCSD ones (see Table S11). CAM-B3LYP*/PDE-X and XsCAM-B3LYP levels give very comparable 2PA strengths, as well. These results emphasize the competitiveness of the cost-efficient XsTD-DFT method for the simulation of 2PA properties of explicitly solvated systems. A more extensive comparison between QM/MM, QM/QM, and XsTD-DFT methods could be the subject of an interesting future work.

This section assessed performances of the XsTD-DFT scheme to compute 1PA and 2PA for microsolvated systems as well as with respect to conventional embedding methods. For the considered microhydrated pNA, thymine, and PYPb chromophores, the XsTD-DFT method consistently gives excitation energies, oscillator strengths, and 2PA strengths in close agreement with the TD-DFT results, following *robustly* EOM-EE-CCSD reference trends. XsTD-DFT excitation energies and oscillator strengths' MADs with respect to EOM-EE-CCSD values are smaller than TD-DFT ones for all the investigated DFAs. For δ^{2PA}, the XsTD-DFT method outperforms TD-DFT by using B3LYP and PBE0 functionals. XsTD-DFT calculations provide very similar results to the CAM-B3LYP*/PDE-X embedding scheme. These results emphasize

https://doi.org/10.1021/acs.jpca.5c03189
J. Phys. Chem. A XXXX, XXX, XXX−XXX

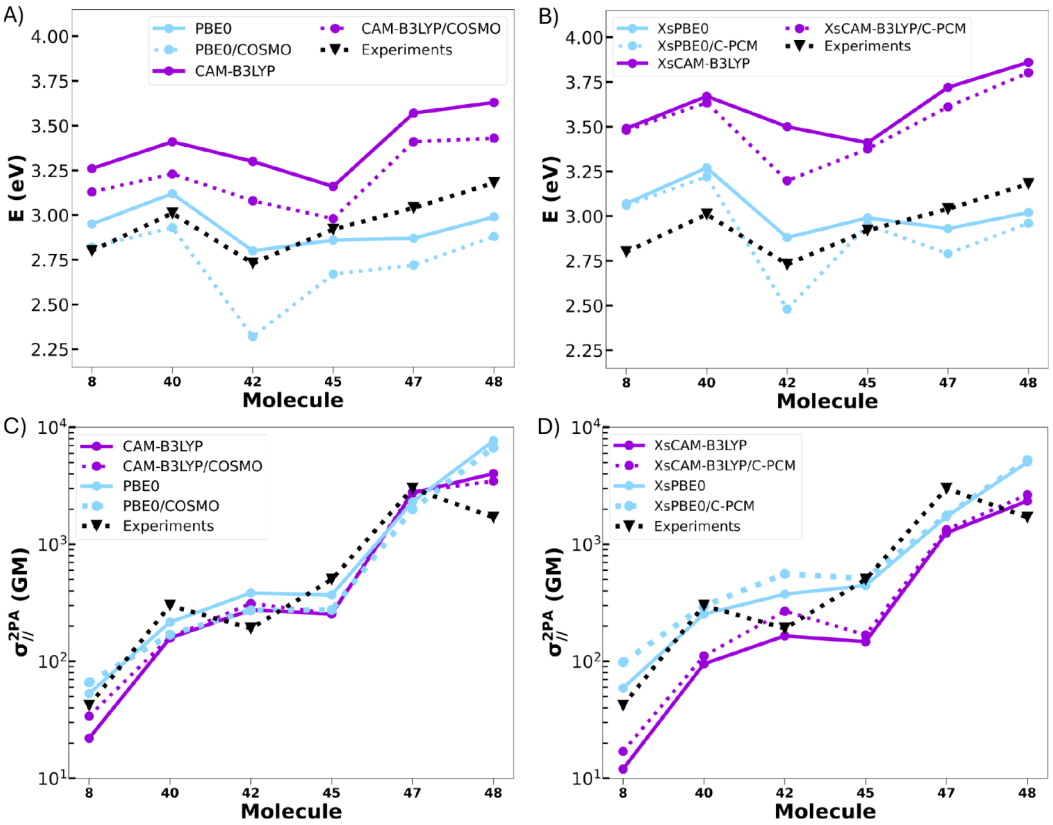

Figure 17. Experimental excitation energies and 2PA cross sections for the 2PA maximum of compounds 8, 40, 45, 47, and 48 recorded in toluene[108,109] and for compound 42 recorded in DMSO[110] in comparison with TD-DFT and XsTD-DFT theoretical ones in vacuum as well as TD-DFT/COSMO and XsTD-DFT/C-PCM. An empirical damping factor of 0.1 eV was used to compute 2PA cross sections, considering a single-beam experiment.

the *cost efficiency* and *reliability* of the XsTD-DFT approach to compute the excited-state properties of explicitly solvated chromophores. For a few systems from the CT set, the next section compares XsTD-DFT results in vacuum and using implicit solvation models to experimental 1PA and 2PA data.

Comparisons with Respect to Available Experimental 1PA and 2PA Data from the CT Set. Among compounds from the CT set, 1PA and 2PA experimental data are available in the literature[108−110] for compounds 8, 40, 45, 47, and 48 in toluene[108,109] as well as for compound 42 in DMSO.[110] All 2PA data were obtained from single-beam experiments.[108−110]

First, to further assess the performance of the XsTD-DFT method, experimental 1PA and 2PA results recorded in solution are compared to TD-DFT and XsTD-DFT results computed in a vacuum. Second, implicit solvent effects are accounted for with COSMO for TD-DFT 2PA calculations preformed with `Turbomole 7.6.1`[102] and C-PCM for XsTD-DFT calculations for which ground states were computed with `Q-Chem 6.0.1.2`.[106] Note that for XsTD-DFT calculations, implicit solvent effects are only accounted for in ground-state calculations. In vacuum, TD-DFT, XsTD-DFT, and RI-CC2 excitation energies and molar absorption coefficients (absorption maximum) already show reasonable agreement with respect to experiments. These results are summarized in Figures S29 and S30. Similar results are also found for the 2PA strengths (Figures S31 and S32). Details on how the molar absorption coefficients (ε) and 2PA cross sections are computed can be found in the Supporting Information. For compounds 40, 45, and 47, Figure S32 compares experimental 2PA spectra[109] to PBE0 and XsPBE0 ones. While solvent and dynamic structural effects are not accounted for, comparisons with respect to experiment remain reasonable, illustrating the suitability of the XsTD-DFT scheme for this purpose.

We now discuss the impact of implicit solvation models on XsTD-DFT and TD-DFT results and how they compare to experimental data. For TD-DFT calculations, we used the simple Conductor-like Screening Model (COSMO)[111−113] implemented in `Turbomole 7.6.1`.[102] The current implementation of the XsTD-DFT scheme in the `std2`[101] software does not include any linear response PCM. Thus, the impact of the solvent is only accounted for through the ground-state Kohn−Sham MOs. For XsTD-DFT calculations, the DFT ground state is computed by using the C-PCM model implemented in QChem 6.0.1.2. For systems 8, 40, 42, 45, 47, and 48, Figure 16 compares TD-DFT and XsTD-DFT excitation energies and molar absorption coefficients to TD-DFT/COSMO and XsTD-DFT/C-PCM ones using PBE0 and CAM-B3LYP exchange−correlation functionals. TD-DFT/COSMO excitation energies are systematically red-shifted with respect to TD-DFT ones. The effect of the solvation model at the PBE0/COSMO level of theory is more significant for system 42 because of the more polar DMSO solvent used. As expected, XsTD-DFT/C-PCM excitation energies are only slightly red-shifted with respect to vacuum energies, with the exception of system 42. Including implicit solvation effects for the ground state seems to improve XsTD-DFT excitation energies for more polar solvents (such as DMSO), improving the comparison of XsTD-DFT trends with experimental ones. Using an implicit solvent model at the TD-DFT level generally results in a slight increase of ε values. XsTD-DFT/C-PCM ε

https://doi.org/10.1021/acs.jpca.5c03189
J. Phys. Chem. A XXXX, XXX, XXX−XXX

values do not differ significantly from those computed in vacuum or exhibit a rather modest tendency toward lower values. 2PA excitation energy trends, passing from vacuum to implicit solvent results, are similar to the 1PA ones, as illustrated in Figure 17. The excitation energies of system 47 (in toluene) computed with XsTD-DFT decrease similarly to those obtained with TD-DFT using an implicit solvent model. The order of magnitude of the 2PA strengths remains largely unaffected when introducing an implicit solvent model for both TD-DFT and XsTD-DFT results.

This section answered questions (4) and (5) outlined in the Introduction, showing how single structure in vacuum XsTD-DFT calculations compare to experimental 1PA and 2PA properties and if introducing an implicit solvent model improves these comparisons. We showed a relatively good agreement between XsTD-DFT 1PA and 2PA results in a vacuum with respect to experiments. Using an implicit solvent model with the XsTD-DFT method improves excitation energies as well as oscillator and 2PA strengths with respect to experiments only for compound 47 in DMSO. Given the computational efficiency of the XsTD-DFT method, AQM methodologies[74] for modeling chromophores explicitly in solution are more appealing for comparison with experimental spectra than implicit solvent models. Moreover, accounting for dynamic structural effects in ADQM protocols[74] is anticipated to further improve the agreement between theory and experiment. These insights underscore the potential of XsTD-DFT for future applications in computing the optical properties of realistic systems.

CONCLUSIONS

sQC methods to compute excited states and response properties can support AQM methodologies to deal with realistic systems, bridging the gap between experimental and computational spectroscopy.[74,75] In this framework, the performance of the XsTD-DFT method was assessed to compute 1PA and 2PA, employing a large database of 91 systems. XsTD-DFT excitation energies, oscillator, and 2PA strengths were compared to RI-CC2 reference calculations as well as TD-DFT ones. sTD-DFT results are also discussed. The present work highlights that the newly developed XsTD-DFT method is *reliable*, providing good agreement with respect to RI-CC2 results. For both 1PA and 2PA, the XsTD-DFT method shows similar agreement with respect to RI-CC2 results as TD-DFT when varying the amount of HFX in the GH functional, but in a *computationally efficient* way, reducing CPU times by 3 orders of magnitude. One downside of the method is its performance in computing 2PA strengths with GH functionals with a large amount of HFX and RSH DFAs. This is currently under investigation in our group. The XsTD-DFT method is also *robust*. It consistently performs well across different types of 1P- and 2P-active systems, demonstrating good error tolerance with respect to RI-CC2 results and, in particular, to TD-DFT ones. In addition, the XsTD-DFT scheme removes the semiempiricism of the sTD-DFT two-electron integrals. The *reliability*, *robustness*, and *computational efficiency* of the XsTD-DFT method are particularly appealing for high-throughput screening and as a key ingredient for AQM workflows.

The introduction outlined five questions to guide the assessment of the XsTD-DFT method for its application to AQM methodologies. This work showed that (1) with respect to TD-DFT and RI-CC2, the XsTD-DFT method can capture trends of excitation energies as well as oscillator and 2PA strengths among subsets of similar compounds; (2) a rigid scan of the dihedral angle for system 1 suggested that the XsTD-DFT method is as reliable as TD-DFT for nonequilibrium geometries, providing *robust* comparisons to RI-CC2 excitation energies and 2PA strengths; (3) XsTD-DFT 1PA and 2PA results are *reliable* also for microsolvated systems, closely following EOM-EE-CCSD trends; (4) comparisons with respect to 1PA and 2PA experimental data indicate that XsTD-DFT calculations in vacuum for few isolated CT molecules already yield reasonable agreements, similar to what is usually achieved by TD-DFT; and (5) for the same systems, simply using an implicit solvent model for the DFT ground-state MOs with the XsTD-DFT calculations has a rather small impact on excitation energies, ε, and σ^{2PA} with respect to experiments, except for system 42 recorded in DMSO. Note that the XsTD-DFT method can be employed in AQM methodologies to treat explicitly solvated systems.[74]

In light of these findings, we suggest the following guidelines to compute 1PA and 2PA with the XsTD-DFT method:

- DFAs with large amount of HFX (e.g., M06-2X or BHandHLYP) should be preferred to compute 1PA with the XsTD-DFT scheme.
- For 2PA, the XsPBE0 level offers a good compromise between reproducing excitation energies and 2PA strengths, especially for CT excited states of 2P-active molecules.
- With respect to the sTD-DFT method, the XsTD-DFT scheme recovers the basis set dependence. The selection of a (double-ζ) basis set for a XsTD-DFT calculation is very similar to the one done for TD-DFT. The largest basis sets investigated here (6-31+G(d) and aug-cc-pVDZ) are recommended to compute excitation energies and δ^{2PA} with the XsTD-DFT scheme. Selecting a proper DFA impacts more XsTD-DFT results than selecting a (double-ζ) basis set when compared to RI-CC2 data. Note that for the largest systems of the CT set (>150 electrons), XsTD-DFT excitation energies converge toward the TD-DFT ones already with the smallest basis sets, i.e., 3-21G(d) and 6-31G(d).
- Regarding the selection of the energy threshold used to truncate the CIS space in the XsTD-DFT procedure, it is generally possible to identify a range of E_{thr} values that yield excitation energies close to the TD-DFT ones since deviations of XsTD-DFT excitation energies from TD-DFT values decrease monotonically. When using GH functionals, $E_{thr} \in [9, 12]$ eV is sufficient to converge to TD-DFT excitation energies, while RSH DFAs, e.g., CAM-B3LYP and ωB97M-V, require larger values (E_{thr} > 12 eV). When selecting an appropriate E_{thr}, it is advisible to choose the lowest value that guarantees convergence, thereby minimizing the number of CSFs and reducing computational cost.

The XsTD-DFT method is implemented in the open-source `std2`[101] software available on GitHub for the community. `std2` adheres to a software development model based on reusable software.[114] The XsTD-DFT implementation uses the `libcint`[107] integral library. `std2` can also be seen as modular and reusable since it can be in principle interfaced with any QC code through standardized `molden` input files. This makes `std2` fit into the sustainable software development environment for electronic structure methods that should be standard for future developments of QC codes.[114,115] The *computational efficiency* of the XsTD-DFT method together with its *robustness*

https://doi.org/10.1021/acs.jpca.5c03189
J. Phys. Chem. A XXXX, XXX, XXX−XXX

and *reliability* opens the door to use the XsTD-DFT scheme as a key ingredient for AQM workflows to compute 1PA and 2PA.

As the scientific community continues to push boundaries of computational spectroscopy, the synergy of advanced methods for excited states, new algorithms, and modern hardware[115] is rapidly transforming what was possible to do. Developments such as linear-scaling[116,117] approaches, quantum embedding techniques,[118] and the adaptation of quantum chemistry codes to GPU architectures[119−121] are laying the ground for simulations of unprecedented scale. Within this landscape, this work highlights the growing importance of sQC methods and in particular the XsTD-DFT scheme as an essential tool for efficient predictions of optical properties for large and realistic systems. We envision that the XsTD-DFT method and related approaches could become central to next-generation computational protocols, driving progress toward the long-standing goal of closing the gap between theory and experimental spectroscopy of molecular systems.

■ ASSOCIATED CONTENT

Supporting Information

The Supporting Information is available free of charge at https://pubs.acs.org/doi/10.1021/acs.jpca.5c03189.

For the QUEST data set, RI-CC2/aug-cc-pVDZ excitation energy and oscillator strength MADs and RMSDs as well as correlation plots with respect to TBE; list of excluded systems from QUEST; for both QUEST and CT sets, excitation energy, oscillator strength, and $\log(\delta^{2PA})$ MADs and RMSDs as well as correlation plots computed at TD-DFT, sTD-DFT, and XsTD-DFT levels of theory using different DFAs as well as at the sTD-DFT-xTB level with respect to the RI-CC2/aug-cc-pVDZ results; excitation energies for the two first excited states (S1 and S2) of phthalazine at TBE/aug-cc-pVTZ and RI-CC2/aug-cc-pVDZ levels in comparison with TD-DFT, sTD-DFT, and XsTD-DFT results; oscillator strengths and transition energies (in eV) of n → π^* states; analysis of basis set effects, including plots reporting MADs for excitation energies, oscillator strengths, and $\log(\delta^{2PA})$ computed at TD-DFT, sTD-DFT, and XsTD-DFT levels of theory considering different basis sets with respect to the RI-CC2/aug-cc-pVDZ results; for both QUEST and CT sets, sTD-DFT and XsTD-DFT absolute deviations from TD-DFT excitation energies and $\log(\delta^{2PA})$ as a function of the number of electrons of the system; analysis of the impact of the truncation of the CIS space on XsTD-DFT results for systems 4, 13, and 34 of the CT set, including the impact of the energy threshold on the CPU time; for system 1 from the CT set, excitation energies, oscillator, and 2PA strengths for the *n* excited state at different dihedral angle values computed with RI-CC2, PBE0, and XsPBE0 levels of theory; for microhydrated systems, excitation energy, oscillator strength, and $\log(\delta^{2PA})$ MADs considering different DFAs at TD-DFT, sTD-DFT, XsTD-DFT, RI-CC2 levels of theory with respect to EOM-EE-CCSD results as well as comparisons for δ^{2PA} with other schemes; a discussion that compares results in vacuum with respect to available experimental 1PA and 2PA data from the CT set; experimental excitation energies, molar absorption coefficients, and 2PA cross sections for the absorption maximum of compounds 8, 40, 45, 47, and 48 recorded toluene as well as for compound 42 recorded in DMSO in comparison with TD-DFT, XsTD-DFT, and RI-CC2 theoretical ones in vacuum; comparisons of computed experimental 1PA and 2PA spectra for selected systems with respect to experimental ones; details about the broadening of computed 1PA and 2PA spectra (PDF)

Excitation energies, oscillator, and 2PA strengths obtained for different DFAs at TD-DFT, sTD-DFT, and XsTD- DFT levels of theory using the aug-cc-pVDZ basis set for QUEST (QUEST_1PA, QUEST_2PA), CT set (CT), and microhydrated systems (microhydrated); results of gauge_mGGA_(RS)H (XLSX)

■ AUTHOR INFORMATION

Corresponding Author

Marc de Wergifosse − *Theoretical Chemistry Group, Molecular Chemistry, Materials and Catalysis Division (MOST), Institute of Condensed Matter and Nanosciences, Université Catholique de Louvain, Louvain-la-Neuve B-1348, Belgium;* orcid.org/0000-0002-9564-7303; Email: marc.dewergifosse@uclouvain.be

Author

Marilù G. Maraldi − *Theoretical Chemistry Group, Molecular Chemistry, Materials and Catalysis Division (MOST), Institute of Condensed Matter and Nanosciences, Université Catholique de Louvain, Louvain-la-Neuve B-1348, Belgium;* orcid.org/0009-0005-3877-6546

Complete contact information is available at: https://pubs.acs.org/10.1021/acs.jpca.5c03189

Notes

The authors declare no competing financial interest.

■ ACKNOWLEDGMENTS

MGM thanks the F.R.S.-FNRS for her Research Fellow position. The authors thank Prof. Robert Zaleśny for his support and for RI-CC2 excitation energies, oscillator strengths, and 2PA strengths of the CT set molecules. Computational resources were provided by the supercomputer facilities at the UCLouvain (CISM) and the Consortium des Équipements de Calcul Intensif en Fédération Wallonie Bruxelles (CÉCI) funded by the Fonds de la Recherche Scientifique de Belgique (F.R.S.-FNRS) under convention 2.5020.11 and the Walloon Region.

■ REFERENCES

(1) Grimme, S. A Simplified Tamm-Dancoff Density Functional Approach for the Electronic Excitation Spectra of Very Large Molecules. *J. Chem. Phys.* **2013**, *138*, 244104.

(2) Bannwarth, C.; Grimme, S. A Simplified Time-Dependent Density Functional Theory Approach for Electronic Ultraviolet and Circular Dichroism Spectra of Very Large Molecules. *Comput. Theor. Chem.* **2014**, *1040−1041*, 45−53.

(3) de Wergifosse, M. Computing Excited States of Very Large Systems with Range-Separated Hybrid Functionals and the eXact Integral Simplified Time-Dependent Density Functional Theory (XsTD-DFT). *J. Phys. Chem. Lett.* **2024**, *15*, 12628−12635.

(4) Göppert-Mayer, M. Elementary Processes with Two Quantum Transitions. *Ann. Phys.* **2009**, *521*, 466−479.

(5) Wehling, A.; Walla, P. J. Time-Resolved Two-Photon Spectroscopy of Photosystem I Determines Hidden Carotenoid Dark-State Dynamics. *J. Phys. Chem. B* **2005**, *109*, 24510−24516.

(6) Forli, A.; Vecchia, D.; Binini, N.; Succol, F.; Bovetti, S.; Moretti, C.; Nespoli, F.; Mahn, M.; Baker, C. A.; Bolton, M. M.; et al. Two-

Photon Bidirectional Control and Imaging of Neuronal Excitability with High Spatial Resolution In Vivo. *Cell Rep.* **2018**, *22*, 3087−3098.
(7) Patterson, G. H.; Piston, D. W. Photobleaching in Two-Photon Excitation Microscopy. *Biophys. J.* **2000**, *78*, 2159−2162.
(8) *Photoresponsive Polymers I*, Marder, S. R.; Lee, K.-S., Eds.; Springer: Berlin Heidelberg, 2008.
(9) Bolze, F.; Jenni, S.; Sour, A.; Heitz, V. Molecular Photosensitisers for Two-photon Photodynamic Therapy. *Chem. Commun.* **2017**, *53*, 12857−12877.
(10) Soleimany, A.; Aghmiouni, D. K.; Amirikhah, M.; Shokrgozar, M. A.; Khoee, S.; Sarmento, B. Two-Photon Mediated Cancer Therapy: A Comprehensive Review on Two-Photon Photodynamic Therapy and Two-Photon-Activated Therapeutic Delivery Systems. *Adv. Funct. Mater.* **2024**, *34*, 2408594.
(11) Wang, H.; Zhang, W.; Ladika, D.; Yu, H.; Gailevičius, D.; Wang, H.; Pan, C.-F.; Nair, P. N. S.; Ke, Y.; Mori, T.; et al. Two-Photon Polymerization Lithography for Optics and Photonics: Fundamentals, Materials, Technologies, and Applications. *Adv. Funct. Mater.* **2023**, *33*, 2214211.
(12) Larson, A. M. Multiphoton Microscopy. *Nat. Photonics* **2011**, *5*, 1.
(13) Sneskov, K.; Olsen, J. M. H.; Schwabe, T.; Hättig, C.; Christiansen, O.; Kongsted, J. Computational Screening of One- and Two-Photon Spectrally Tuned Channelrhodopsin Mutants. *Phys. Chem. Chem. Phys.* **2013**, *15*, 7567−7576.
(14) Matczyszyn, K.; Olesiak-Banska, J.; Nakatani, K.; Yu, P.; Murugan, N. A.; Zaleśny, R.; Roztoczyńska, A.; Bednarska, J.; Bartkowiak, W.; Kongsted, J.; et al. One- and Two-Photon Absorption of a Spiropyran-Merocyanine System: Experimental and Theoretical Studies. *J. Phys. Chem. B* **2015**, *119*, 1515−1522.
(15) Khan, M. U.; Mehboob, M. Y.; Hussain, R.; Fatima, R.; Tahir, M. S.; Khalid, M.; Braga, A. A. C. Molecular Designing of High-Performance 3D Star-Shaped Electron Acceptors Containing a Truxene Core for Nonfullerene Organic Solar Cells. *J. Phys. Org. Chem.* **2021**, *34*, No. e4119.
(16) Olsen, J.; Jo/rgensen, P. Linear and Nonlinear Response Functions for an Exact State and for an MCSCF State. *J. Chem. Phys.* **1985**, *82*, 3235−3264.
(17) Silva, D. L.; Barreto, R. C.; Lacerda, E.; Coutinho, K.; Canuto, S. One- and Two-Photon Absorption of Fluorescein Dianion in Water: A Study Using S-QM/MM Methodology and ZINDO Method. *Spectrochim. Acta, Part A* **2014**, *119*, 63−75.
(18) Serrano-Andrés, L.; Merchán, M. Quantum Chemistry of the Excited State: 2005 overview. *J. Mol. Struct.: Theochem* **2005**, *729*, 99−108. Proceedings of the 30th International Congress of Theoretical Chemists of Latin Expression
(19) Kimber, P.; Plasser, F. *Comprehensive Computational Chemistry*, 1st ed.; Elsevier, 2024. pp 55-83.
(20) Hättig, C.; Christiansen, O.; Jo/rgensen, P. Coupled Cluster Response Calculations of Two-Photon Transition Probability Rate Constants for Helium, Neon and Argon. *J. Chem. Phys.* **1998**, *108*, 8355−8359.
(21) Nanda, K. D.; Krylov, A. I. Two-photon Absorption Cross Sections within Equation-Of-Motion Coupled-Cluster Formalism Using Resolution-of-the-Identity and Cholesky Decomposition Representations: Theory, Implementation, and Benchmarks. *J. Chem. Phys.* **2015**, *142*, 064118.
(22) Paterson, M. J.; Christiansen, O.; Pawłowski, F.; Jørgensen, P.; Hättig, C.; Helgaker, T.; Sałek, P. Benchmarking Two-Photon Absorption with CC3 Quadratic Response Theory, and Comparison with Density-Functional Response Theory. *J. Chem. Phys.* **2006**, *124*, 054322.
(23) Friese, D. H.; Hättig, C.; Ruud, K. Calculation of Two-Photon Absorption Strengths with the Approximate Coupled Cluster Singles and Doubles Model CC2 Using the Resolution-of-Identity Approximation. *Phys. Chem. Chem. Phys.* **2012**, *14*, 1175−1184.
(24) Zahariev, F.; Gordon, M. S. Nonlinear Response Time-Dependent Density Functional Theory Combined with the Effective Fragment Potential Method. *J. Chem. Phys.* **2014**, *140*, 18A523.
(25) Parker, S. M.; Rappoport, D.; Furche, F. Quadratic Response Properties from TDDFT: Trials and Tribulations. *J. Chem. Theory Comput.* **2018**, *14*, 807−819.
(26) de Wergifosse, M.; Houk, A. L.; Krylov, A. I.; Elles, C. G. Two-photon Absorption Spectroscopy of trans-Stilbene, cis-Stilbene, and Phenanthrene: Theory and Experiment. *J. Chem. Phys.* **2017**, *146*, 144305.
(27) de Wergifosse, M.; Elles, C. G.; Krylov, A. I. Two-photon Absorption Spectroscopy of Stilbene and Phenanthrene: Excited-State Analysis and Comparison with Ethylene and Toluene. *J. Chem. Phys.* **2017**, *146*, 174102.
(28) Naim, C.; Zaleśny, R.; Jacquemin, D. Two-Photon Absorption Strengths of Small Molecules: Reference CC3 Values and Benchmarks. *J. Chem. Theory Comput.* **2024**, *20*, 9093−9106.
(29) Suellen, C.; Freitas, R. G.; Loos, P.-F.; Jacquemin, D. Cross-Comparisons between Experiment, TD-DFT, CC, and ADC for Transition Energies. *J. Chem. Theory Comput.* **2019**, *15*, 4581−4590.
(30) Laurent, A. D.; Jacquemin, D. TD-DFT benchmarks: A review. *Int. J. Quantum Chem.* **2013**, *113*, 2019−2039.
(31) Beerepoot, M. T. P.; Friese, D. H.; List, N. H.; Kongsted, J.; Ruud, K.; Benchmarking Two-Photon Absorption Cross Sections: Performance of CC2 and CAM-B3LYP. *Phys. Chem. Chem. Phys.* 19306−19314. .
(32) Beerepoot, M. T. P.; Alam, M. M.; Bednarska, J.; Bartkowiak, W.; Ruud, K.; Zaleśny, R. Benchmarking the Performance of Exchange-Correlation Functionals for Predicting Two-Photon Absorption Strengths. *J. Chem. Theory Comput.* **2018**, *14*, 3677−3685.
(33) Choluj, M.; Alam, M. M.; Beerepoot, M. T. P.; Sitkiewicz, S. P.; Matito, E.; Ruud, K.; Zaleśny, R. Choosing Bad versus Worse: Predictions of Two-Photon-Absorption Strengths Based on Popular Density Functional Approximations. *J. Chem. Theory Comput.* **2022**, *18*, 1046−1060.
(34) Ahmadzadeh, K.; Li, X.; Rinkevicius, Z.; Norman, P.; Zaleśny, R. Toward Accurate Two-Photon Absorption Spectrum Simulations: Exploring the Landscape beyond the Generalized Gradient Approximation. *J. Phys. Chem. Lett.* **2024**, *15*, 969−974.
(35) Salek, P.; Vahtras, O.; Guo, J.; Luo, Y.; Helgaker, T.; Ågren, H. Calculations of Two-Photon Absorption Cross Sections by Means of Density-Functional Theory. *Chem. Phys. Lett.* **2003**, *374*, 446−452.
(36) Casida, M. E.; Chong, D. P. *Recent Advances in Density Functional Methods Part I*; World Scientific: Singapore, 1995.
(37) Elliott, P.; Goldson, S.; Canahui, C.; Maitra, N. T. Perspectives on Double-Excitations in TDDFT. *Chem. Phys.* **2011**, *391*, 110−119.
(38) Champagne, B.; Perpéte, E. A.; van Gisbergen, S. J. A.; Baerends, E.-J.; Snijders, J. G.; Soubra-Ghaoui, C.; Robins, K. A.; Kirtman, B. Assessment of Conventional Density Functional Schemes for Computing the Polarizabilities and Hyperpolarizabilities of Conjugated Oligomers: An Ab Initio Investigation of Polyacetylene Chains. *J. Chem. Phys.* **1998**, *109*, 10489−10498.
(39) Peach, M. J. G.; Benfield, P.; Helgaker, T.; Tozer, D. J. Excitation Energies in Density Functional Theory: An Evaluation and a Diagnostic Test. *J. Chem. Phys.* **2008**, *128*, 044118.
(40) List, N. H.; Olsen, J. M.; Rocha-Rinza, T.; Christiansen, O.; Kongsted, J. Performance of Popular XC-Functionals for the Description of Excitation Energies in GFP-like Chromophore Models. *Int. J. Quantum Chem.* **2012**, *112*, 789−800.
(41) Isegawa, M.; Peverati, R.; Truhlar, D. G. Performance of Recent and High-Performance Approximate Density Functionals for Time-Dependent Density Functional Theory Calculations of Valence and Rydberg Electronic Transition Energies. *J. Chem. Phys.* **2012**, *137*, 244104.
(42) Liang, J.; Feng, X.; Hait, D.; Head-Gordon, M. Revisiting the Performance of Time-Dependent Density Functional Theory for Electronic Excitations: Assessment of 43 Popular and Recently Developed Functionals from Rungs One to Four. *J. Chem. Theory Comput.* **2022**, *18*, 3460−3473.
(43) Adamo, C.; Jacquemin, D. The Calculations of Excited-State Properties with Time-Dependent Density Functional Theory. *Chem. Soc. Rev.* **2013**, *42*, 845−856.

https://doi.org/10.1021/acs.jpca.5c03189
J. Phys. Chem. A XXXX, XXX, XXX−XXX

(44) Hall, D.; Sancho-GarcÍa, J. C.; Pershin, A.; Beljonne, D.; Zysman-Colman, E.; Olivier, Y. Benchmarking DFT Functionals for Excited-State Calculations of Donor-Acceptor TADF Emitters: Insights on the Key Parameters Determining Reverse Inter-System Crossing. *J. Phys. Chem. A* **2023**, *127*, 4743−4757.
(45) *Reviews in Computational Chemistry*, Parrill, A. L.; Lipkowitz, K. B., Eds.; John Wiley I& Sons, Ltd, 2017.
(46) Elayan, I. A.; Rib, L.; Mendes, R. A.; Brown, A. Beyond Explored Functionals: A Computational Journey of Two-Photon Absorption. *J. Chem. Theory Comput.* **2024**, *20*, 3879−3893.
(47) Grotjahn, R.; Furche, F. Gauge-Invariant Excited-State Linear and Quadratic Response Properties within the Meta-Generalized Gradient Approximation. *J. Chem. Theory Comput.* **2023**, *19*, 4897−4911.
(48) Grotjahn, R.; Furche, F.; Kaupp, M. Importance of Imposing Gauge Invariance in Time-Dependent Density Functional Theory Calculations with Meta-Generalized Gradient Approximations. *J. Chem. Phys.* **2022**, *157*, 111102.
(49) Grotjahn, R.; Furche, F. C. Comment on Toward Accurate Two-Photon Absorption Spectrum Simulations: Exploring the Landscape beyond the Generalized Gradient Approximation. *J. Phys. Chem. Lett.* **2024**, *15*, 6237−6240.
(50) Zuehlsdorff, T. J.; Isborn, C. M. Modeling Absorption Spectra of Molecules in Solution. *Int. J. Quantum Chem.* **2019**, *119*, No. e25719.
(51) Sarkar, R.; Naim, C.; Ahmadzadeh, K.; Zaleśny, R.; Jacquemin, D.; Luis, J. M. Simulations of Two-Photon Absorption Spectra of Fluorescent Dyes: The Impact of Non-Condon Effects. *J. Chem. Theory Comput.* **2025**, *21*, 3587−3599.
(52) Bishop, D. M.; Luis, J. M.; Kirtman, B. Vibration and Two-photon Absorption. *J. Chem. Phys.* **2002**, *116*, 9729−9739.
(53) Silverstein, D. W.; Jensen, L. Vibronic Coupling Simulations for Linear and Nonlinear Optical Processes: Theory. *J. Chem. Phys.* **2012**, *136*, 064111.
(54) Lin, N.; Luo, Y.; Ruud, K.; Zhao, X.; Santoro, F.; Rizzo, A. Differences in Two-Photon and One-Photon Absorption Profiles Induced by Vibronic Coupling: The Case of Dioxaborine Heterocyclic Dye. *ChemPhyschem* **2011**, *12*, 3392−3403.
(55) Kamarchik, E.; Krylov, A. I. Non-Condon Effects in the One- and Two-Photon Absorption Spectra of the Green Fluorescent Protein. *J. Phys. Chem. Lett.* **2011**, *2*, 488−492.
(56) Macak, P.; Luo, Y.; Norman, P.; Ågren, H. Electronic and Vibronic Contributions to Two-Photon Absorption of Molecules with Multi-Branched Structures. *J. Chem. Phys.* **2000**, *113*, 7055−7061.
(57) Avila Ferrer, F. J.; Santoro, F. Comparison of Vertical and Adiabatic Harmonic Approaches for the Calculation of the Vibrational Structure of Electronic Spectra. *Phys. Chem. Chem. Phys.* **2012**, *14*, 13549−13563.
(58) Giovannini, T.; Cappelli, C. Continuum vs. Atomistic Approaches to Computational Spectroscopy of Solvated Systems. *Chem. Commun.* **2023**, *59*, 5644−5660.
(59) Mennucci, B.; Corni, S. Multiscale Modelling of Photoinduced Processes in Composite Systems. *Nat. Rev. Chem.* **2019**, *3*, 315−330.
(60) Avagliano, D.; Conti, I.; El-Tahawy, M. M.; Jaiswal, V. K.; Nenov, A.; Garavelli, M. In *Comprehensive Computational Chemistry*, 1st ed.; Yáñez, M.; Boyd, R. J.; Elsevier: Oxford, 2024; pp. 158−187.
(61) Warshel, A.; Levitt, M. Theoretical Studies of Enzymic Reactions: Dielectric, Electrostatic and Steric Stabilization of the Carbonium Ion in the Reaction of Lysozyme. *J. Mol. Biol.* **1976**, *103*, 227−249.
(62) Sepali, C.; Gómez, S.; Grifoni, E.; Giovannini, T.; Cappelli, C. Computational Spectroscopy of Aqueous Solutions: The Underlying Role of Conformational Sampling. *J. Phys. Chem. B* **2024**, *128*, 5083−5091.
(63) Jing, Z.; Liu, C.; Cheng, S. Y.; Qi, R.; Walker, B. D.; Piquemal, J.-P.; Ren, P. Polarizable Force Fields for Biomolecular Simulations: Recent Advances and Applications. *Annu. Rev. Biophys.* **2019**, *48*, 371−394.
(64) Curutchet, C.; Mennucci, B. Quantum Chemical Studies of Light Harvesting. *Chem. Rev.* **2017**, *117*, 294−343.
(65) Avagliano, D.; Tkaczyk, S.; Sánchez-Murcia, P. A.; González, L. Enhanced Rigidity Changes Ultraviolet Absorption: Effect of a Merocyanine Binder on G-Quadruplex Photophysics. *J. Phys. Chem. Lett.* **2020**, *11*, 10212−10218.
(66) Mennucci, B. Modeling Absorption and Fluorescence Solvatochromism with QM/Classical Approaches. *Int. J. Quantum Chem.* **2015**, *115*, 1202−1208.
(67) Rossano-Tapia, M.; Olsen, J. M. H.; Brown, A. Two-Photon Absorption Cross-Sections in Fluorescent Proteins Containing Non-canonical Chromophores Using Polarizable QM/MM. *Front. Mol. Biosci.* **2020**, *7*, 111.
(68) Ramos, T. N.; Franco, L. R.; Silva, D. L.; Canuto, S. Calculation of the One- and Two-photon Absorption Spectra of Water-Soluble Stilbene Derivatives Using a Multiscale QM/MM Approach. *J. Chem. Phys.* **2023**, *159*, 024309.
(69) Nanda, K. D.; Krylov, A. I. The Effect of Polarizable Environment on Two-Photon Absorption Cross Sections Characterized by the Equation-of-Motion Coupled-Cluster Singles and Doubles Method Combined with the Effective Fragment Potential Approach. *J. Chem. Phys.* **2018**, *149*, 164109.
(70) Attia, A. A. A.; Reinholdt, P.; Kongsted, J. Modeling One- and Two-Photon Excitation of 4′Hydroxymethyl)-4,5′8-trimethylpsoralen in Complex with DNA: Solving Electron Spill-Out Problems in Polarizable QM/MM Calculations. *Adv. Theory Simul.* **2021**, *4*, 2000294.
(71) Gordon, M. S.; Freitag, M. A.; Bandyopadhyay, P.; Jensen, J. H.; Kairys, V.; Stevens, W. J. The Effective Fragment Potential Method: a QM-Based MM Approach to Modeling Environmental Effects in Chemistry. *J. Phys. Chem. A* **2001**, *105*, 293−307.
(72) Milanese, J. M.; Provorse, M. R.; Alameda, E. J.; Isborn, C. M. Convergence of Computed Aqueous Absorption Spectra with Explicit Quantum Mechanical Solvent. *J. Chem. Theory Comput.* **2017**, *13*, 2159−2171.
(73) Löffelsender, S.; Beaujean, P.; de Wergifosse, M. Simplified Quantum Chemistry Methods to Evaluate Non-Linear Optical Properties of Large Systems. *Wiley Interdiscip. Rev.: comput. Mol. Sci.* **2024**, *14*, No. e1695.
(74) Löffelsender, S.; Maraldi, M. G.; de Wergifosse, M. All-Atom Quantum Mechanical (AQM) Methodologies to Evaluate One- and Two-Photon Absorption of Realistic Systems. *ChemPhyschem* **2025**, *26*, 2401121.
(75) Beaujean, P.; Champagne, B.; Grimme, S.; de Wergifosse, M. All-Atom Quantum Mechanical Calculation of the Second-Harmonic Generation of Fluorescent Proteins. *J. Phys. Chem. Lett.* **2021**, *12*, 9684−9690.
(76) de Wergifosse, M.; Beaujean, P.; Grimme, S. Ultrafast Evaluation of Two-Photon Absorption with Simplified Time-Dependent Density Functional Theory. *J. Phys. Chem. A* **2022**, *126*, 7534−7547.
(77) Bannwarth, C.; Ehlert, S.; Grimme, S. GFN2-xTB-An Accurate and Broadly Parametrized Self-Consistent Tight-Binding Quantum Chemical Method with Multipole Electrostatics and Density-Dependent Dispersion Contributions. *J. Chem. Theory Comput.* **2019**, *15*, 1652−1671.
(78) Grimme, S.; Bannwarth, C. Ultra-Fast Computation of Electronic Spectra for Large Systems by Tight-Binding Based Simplified Tamm-Dancoff Approximation (sTDA-xTB). *J. Chem. Phys.* **2016**, *145*, 054103.
(79) de Wergifosse, M.; Grimme, S. Nonlinear-Response Properties in a Simplified Time-Dependent Density Functional Theory (sTD-DFT) Framework: Evaluation of the First Hyperpolarizability. *J. Chem. Phys.* **2018**, *149*, 024108.
(80) de Wergifosse, M.; Seibert, J.; Grimme, S. Simplified Time-Dependent Density Functional Theory (sTD-DFT) for Molecular Optical Rotation. *J. Chem. Phys.* **2020**, *153*, 084116.
(81) de Wergifosse, M.; Grimme, S. Nonlinear-Response Properties in a Simplified Time-Dependent Density Functional Theory (sTD-DFT) Framework: Evaluation of Excited-State Absorption Spectra. *J. Chem. Phys.* **2019**, *150*, 094112.

https://doi.org/10.1021/acs.jpca.5c03189
J. Phys. Chem. A XXXX, XXX, XXX−XXX

(82) de Wergifosse, M.; Bannwarth, C.; Grimme, S. A Simplified Spin-Flip Time-Dependent Density Functional Theory Approach for the Electronic Excitation Spectra of Very Large Diradicals. *J. Phys. Chem. A* **2019**, *123*, 5815−5825.
(83) de Wergifosse, M.; Grimme, S. Perspective on Simplified Quantum Chemistry Methods for Excited States and Response Properties. *J. Phys. Chem. A* **2021**, *125*, 3841−3851.
(84) Bauernschmitt, R.; Ahlrichs, R. Treatment of Electronic Excitations within the Adiabatic Approximation of Time Dependent Density Functional Theory. *Chem. Phys. Lett.* **1996**, *256*, 454−464.
(85) Chen, G. P.; Voora, V. K.; Agee, M. M.; Balasubramani, S. G.; Furche, F. Random-Phase Approximation Methods. *Annu. Rev. Phys. Chem.* **2017**, *68*, 421−445.
(86) Kollmar, C.; Böhm, M. C. An Analysis of the Zero Differential Overlap Approximation. Towards an Improved Semiempirical MO Method Beyond It. *Theoret. Chim. Acta* **1995**, *92*, 13−47.
(87) Husch, T.; Vaucher, A. C.; Reiher, M. Semiempirical Molecular Orbital Models Based on the Neglect of Diatomic Differential Overlap Approximation. *Int. J. Quantum Chem.* **2018**, *118*, No. e25799.
(88) Löwdin, P.-O. On the Nonorthogonality Problem. *Adv. Quantum Chem.* **1970**, *5*, 185−199.
(89) Mataga, N.; Nishimoto, K. Electronic Structure and Spectra of Some Nitrogen Heterocycles. *Z. Phys. Chem.* **1957**, *12*, 140−157.
(90) Ohno, K. Some Remarks on the Pariser-Parr-Pople Method. *Theor. Chim. Acta* **1964**, *2*, 219−227.
(91) Klopman, G. A Semiempirical Treatment of molecular Structures. II. Molecular Terms and Application to diatomic Molecules. *J. Am. Chem. Soc.* **1964**, *86*, 4550−4557.
(92) de Wergifosse, M.; Grimme, S. The eXact Integral Simplified Time-Dependent Density Functional Theory (XsTD-DFT). *J. Chem. Phys.* **2024**, *160*, 204110.
(93) Risthaus, T.; Hansen, A.; Grimme, S. Excited States Using the Simplified Tamm-Dancoff-Approach for Range-Separated Hybrid Density Functionals: Development and Application. *Phys. Chem. Chem. Phys.* **2014**, *16*, 14408−14419.
(94) Véril, M.; Scemama, A.; Caffarel, M.; Lipparini, F.; Boggio-Pasqua, M.; Jacquemin, D.; Loos, P.-F. QUESTDB: A Database of Highly Accurate Excitation Energies for the Electronic Structure Community. *Wiley Interdiscip. Rev.: comput. Mol. Sci.* **2021**, *11*, No. e1517.
(95) Loos, P.-F.; Comin, M.; Blase, X.; Jacquemin, D. Reference Energies for Intramolecular Charge-Transfer Excitations. *J. Chem. Theory Comput.* **2021**, *17*, 3666−3686.
(96) Loos, P.-F.; Jacquemin, D. A Mountaineering Strategy to Excited States: Highly Accurate Energies and Benchmarks for Bicyclic Systems. *J. Phys. Chem. A* **2021**, *125*, 10174−10188.
(97) Larsson, E. D.; Reinholdt, P.; Hedegård, E. D.; Kongsted, J. Accuracy of One- and Two-Photon Intensities with the Extended Polarizable Density Embedding Model. *J. Phys. Chem. B* **2023**, *127*, 9905−9914.
(98) Slipchenko, L. V. Solvation of the Excited States of Chromophores in Polarizable Environment: Orbital Relaxation versus Polarization. *J. Phys. Chem. A* **2010**, *114*, 8824−8830.
(99) Khistyaev, K.; Bravaya, K. B.; Kamarchik, E.; Kostko, O.; Ahmed, M.; Krylov, A. I. The Effect of Microhydration on Ionization Energies of Thymine. *Faraday Discuss* **2011**, *150*, 313−330.
(100) Zuev, D.; Bravaya, K. B.; Makarova, M. V.; Krylov, A. I. Effect of Microhydration on the Electronic Structure of the Chromophores of the Photoactive Yellow and Green Fluorescent Proteins. *J. Chem. Phys.* **2011**, *135*, 194304.
(101) std2 (version 2.0.1). *A Program for Computing Excited States and Response Functions via Simplified TD-DFT Methods (sTDA, sTD-DFT, SF-sTD-DFT, XsTDA, XsTD-DFT, and SF-Xs-TD-DFT)*; GitHub, Inc., 2025.
(102) Balasubramani, S. G.; Chen, G. P.; Coriani, S.; Diedenhofen, M.; Frank, M. S.; Franzke, Y. J.; Furche, F.; Grotjahn, R.; Harding, M. E.; Hättig, C.; et al. TURBOMOLE: Modular Program Suite for ab initio Quantum-Chemical and Condensed-Matter Simulations. *J. Chem. Phys.* **2020**, *152*, 184107.
(103) Rumi, M.; Perry, J. W. Two-photon Absorption: An Overview of Measurements and Principles. *Adv. Opt. Photon.* **2010**, *2*, 451−518.
(104) McClain, W. M. Two-Photon Molecular Spectroscopy. *Acc. Chem. Res.* **1974**, *7*, 129−135.
(105) Alam, M.; Chattopadhyaya, M.; Chakrabarti, S.; Ruud, K. Chemical Control of Channel Interference in Two-Photon Absorption Processes. **2014**, *47*, 1604−1612. .
(106) Epifanovsky, E.; Gilbert, A. T. B.; Feng, X.; Lee, J.; Mao, Y.; Mardirossian, N.; Pokhilko, P.; White, A. F.; Coons, M. P.; Dempwolff, A. L.; et al. Software for the Frontiers of Quantum Chemistry: An Overview of Developments in the Q-Chem 5 Package. *J. Chem. Phys.* **2021**, *155*, 084801.
(107) Sun, Q. Libcint: An efficient general integral library for Gaussian basis functions. *J. Comput. Chem.* **2015**, *36*, 1664−1671.
(108) Cao, D.-X.; Fang, Q.; Wang, D.; Liu, Z.-Q.; Xue, G.; Xu, G.-B.; Yu, W.-T. Synthesis and Two-Photon-Excited Fluorescence of Benzothiazole-Based Compounds with Various π-Electron Donors. *Eur. J. Org. Chem.* **2003**, *2003*, 3628−3636.
(109) Strehmel, B.; Sarker, A. M.; Detert, H. The Influence of σ and π Acceptors on Two-Photon Absorption and Solvatochromism of Dipolar and Quadrupolar Unsaturated Organic Compounds. *ChemPhyschem* **2003**, *4*, 249−259.
(110) Antonov, L.; Kamada, K.; Ohta, K.; Kamounah, F. S. A Systematic Femtosecond Study on the Two-Photon Absorbing D-π-A Molecules-π-bridge Nitrogen Insertion and Strength of the Donor and Acceptor Groups. *Phys. Chem. Chem. Phys.* **2003**, *5*, 1193−1197.
(111) Klamt, A.; Schüürmann, G. COSMO: A New Approach to Dielectric Screening in Solvents with Explicit Expressions for the Screening Energy and its Gradient. *J. Chem. Soc., Perkin Trans. 2* **1993**, *2*, 799−805.
(112) Klamt, A. Calculation of UV/Vis Spectra in Solution. *J. Phys. Chem.* **1996**, *100*, 3349−3353.
(113) Schäfer, A.; Klamt, A.; Sattel, D.; Lohrenz, J. C. W.; Eckert, F. COSMO Implementation in TURBOMOLE: Extension of an Efficient Quantum Chemical Code Towards Liquid Systems. *Phys. Chem. Chem. Phys.* **2000**, *2*, 2187−2193.
(114) Lehtola, S. A Call to Arms: Making the Case for More Reusable Libraries. *J. Chem. Phys.* **2023**, *159*, 180901.
(115) Blum, V.; Asahi, R.; Autschbach, J.; Bannwarth, C.; Bihlmayer, G.; Blügel, S.; Burns, L. A.; Crawford, T. D.; Dawson, W.; de Jong, W. A.; et al. Roadmap on Methods and Software for Electronic Structure Based Simulations in Chemistry and Materials. *Electron. Struct.* **2024**, *6*, 042501.
(116) Bowler, D. R.; Miyazaki, T. Methods in Electronic Structure Calculations. *Rep. Prog. Phys.* **2012**, *75*, 036503.
(117) Zuehlsdorff, T. J.; Haynes, P. D.; Hanke, F.; Payne, M. C.; Hine, N. D. M. Solvent Effects on Electronic Excitations of an Organic Chromophore. *J. Chem. Theory Comput.* **2016**, *12*, 1853−1861.
(118) Wouters, S.; Jiménez-Hoyos, C. A.; Chan, G. K.-L. *FragmentationChapter*; John Wiley I& Sons, Ltd, 2017, Vol. *8*, pp. 227−243.
(119) Isborn, C. M.; Luehr, N.; Ufimtsev, I. S.; MartÍnez, T. J. Excited-State Electronic Structure with Configuration Interaction Singles and Tamm-Dancoff Time-Dependent Density Functional Theory on Graphical Processing Units. *J. Chem. Theory Comput.* **2011**, *7*, 1814−1823.
(120) Kim, I.; Jeong, D.; Son, W.-J.; Kim, H.-J.; Rhee, Y. M.; Jung, Y.; Choi, H.; Yim, J.; Jang, I.; Kim, D. S. Kohn-Sham Time-Dependent Density Functional Theory with Tamm-Dancoff Approximation on Massively Parallel GPUs. *Npj Comput. Mater.* **2023**, *9*, 81.
(121) Kim, I.; Jeong, D.; Weisburn, L. P.; Alexiu, A.; Van Voorhis, T.; Rhee, Y. M.; Son, W.-J.; Kim, H.-J.; Yim, J.; Kim, S.; et al. Very-Large-Scale GPU-Accelerated Nuclear Gradient of Time-Dependent Density Functional Theory with Tamm-Dancoff Approximation and Range-Separated Hybrid Functionals. *J. Chem. Theory Comput.* **2024**, *20*, 9018−9031.

https://doi.org/10.1021/acs.jpca.5c03189
J. Phys. Chem. A XXXX, XXX, XXX−XXX